Geosciences

AIMS Geosciences, 11(1): 117–154.
DOI: 10.3934/geosci.2025007
Received: 29 November 2024
Revised: 21 February 2025
Accepted: 04 March 2025
Published: 13 March 2025

https://www.aimspress.com/journal/geosciences

Research article

BIOSPHERE measurement campaign from January 2024 to March 2024 and in May 2024: Effects of the solar events on the radiation belts, UV radiation and ozone in the atmosphere

Viviane Pierrard[1,2,*], David Bolsée[1], Alexandre Winant[1,2], Amer Al-Qaaod[3], Faton Krasniqi[3], Maximilien Péters de Bonhome[1,4], Edith Botek[1], Lionel Van Laeken[1], Danislav Sapundjiev[1,5], Roeland Van Malderen[5], Alexander Mangold[5], Iva Ambrozova[6], Marek Sommer[6], Jakub Slegl[6,7], Styliani A Geronikolou[8,9], Alexandros G Georgakilas[10], Alexander Dorn[11], Benjamin Rapp[12], Jaroslav Solc[13], Lukas Marek[14], Cristina Oancea[14], Lionel Doppler[15], Ronald Langer[16], Sarah Walsh[17], Marco Sabia[17], Marco Vuolo[18], Alex Papayannis[19,20] and Carlos Granja[21,14]

[1] Solar-Terrestrial Center of Excellence, Royal Belgian Institute for Space Aeronomy (BIRA-IASB), Brussels, Belgium
[2] Earth and Life Institute—Climate Sciences (ELI-C), Université Catholique de Louvain, Louvain-la-Neuve, Belgium
[3] Physikalisch-Technische Bundesanstalt (PTB), Bundesallee 100, Braunschweig, Germany
[4] Centre for Mathematical Plasma Astrophysics, Katholiek Universiteit Leuven, Leuven, Belgium
[5] Royal Meteorological Institute of Belgium (IRM-KMI), Brussels, Belgium
[6] Nuclear Physics Institute of the Czech Academy of Sciences, Rez, Czech Republic
[7] Faculty of Nuclear Sciences and Physical Engineering, Czech Technical University, Prague, Czech Republic
[8] University Research Institute of Maternal & child Health & Precision Medicine, National & Kapodistrian University of Athens, Medical School, Athens, Greece
[9] Biomedical Research Foundation of the Academy of Athens, Athens, Greece
[10] DNA Damage Laboratory, Department of Physics School of Applied Mathematical and Physical Sciences, National Technical University of Athens (NTUA), Athens, Greece
[11] MPG MPIK: Max Planck Institute for Nuclear Physics, Heidelberg, Germany
[12] Université Paris-Saclay, CEA, List, Laboratoire National Henri Becquerel (LNE-LNHB), F-91129, Palaiseau, France

[13] Czech Metrology Institute (CMI), Brno, Czech Republic
[14] ADVACAM, Prague, Czech Republic
[15] DWD, MOL-RAO Deutscher Wetterdienst, Meteorologisches Observatorium Lindenberg—Richard-Aßmann-Observatorium, Lindenberg (Tauche), Germany
[16] Institute of Experimental Physics, Slovak Academy of Sciences, Košice, Slovak Republic
[17] Eutelsat, One Web, London, United Kingdom
[18] European Space Agency (ESA), European Space Research and Technology Centre (ESTEC), Noordwijk, The Netherlands
[19] Laser Remote Sensing Unit, Department of Physics, National & Technical University of Athens, Zografou, Greece
[20] Laboratory of Atmospheric Processes and their Impacts, Ecole Polytechnique Fédérale de Lausanne, Lausanne, Switzerland
[21] VSB Technical University of Ostrava, Ostrava, Czech Republic

* **Correspondence:** Email: viviane.pierrard@aeronomie.be; Tel: +32-2-373-0365; Fax: +32-2-374-8423.

Abstract: In this work, we analyzed simultaneous observations of solar particles and solar electromagnetic ultraviolet (UV) radiation during solar events from January 2024 to May 2024. Measurement campaigns to study the effects of space radiation on the terrestrial atmosphere were conducted in the framework of the project BIOSPHERE. We show the results of the campaign in Brussels from 1 January 2024 to 31 March 2024, during which several solar energetic particle (SEP) events were observed by the spacecraft GOES and OMNI, together with two big geomagnetic storms in March 2024 and May 2024 associated with solar eruptions. The last two events combine the arrival of a SEP event with a geomagnetic storm. On 11 May 2024, the biggest geomagnetic storm for the last 20 years was observed. These events enabled us to identify effects due to UV, solar particles, and geomagnetic storms. The impact of these events on the terrestrial radiation belts, illustrated by satellite observations like PROBA-V/EPT and on the atmospheric ozone using AURA/MLS is demonstrated. For the measurement campaign, muon and neutron monitors showed a Forbush decrease only during the geomagnetic storm at the end of March 2024 and in May 2024. Complemented by a simulation of radiation effects on the ionization rate of the atmosphere as a function of the altitude, the extensive range of different observations available during this measurement campaign demonstrated that SEP and geomagnetic storms due to solar eruptions had very different effects on the terrestrial atmosphere. The geomagnetic storms mainly modified the energetic electrons trapped in the space environment of the Earth and affected the ionization of the atmosphere above 60 km. They also modified the cosmic ray injections, mainly at high latitudes, creating Forbush decrease for the most intense ones. SEP events injected energetic protons in the atmosphere that could penetrate deeper in the atmosphere because they had more energy than the electrons. They could impact ozone, mainly at high altitude in the thermosphere. Solar activity variation associated with the rotation of the solar active regions in 27 days modulated UV. The measurements of these electromagnetic and particle radiations are crucial because they have important health implications.

Keywords: space radiation; cosmic rays; ultraviolet; ozone; solar event; radiation belts; Forbush decrease; ionization; neutron monitors; health.

1. Introduction: The BIOSPHERE project

An increased atmospheric ionization by cosmic rays and solar UV radiation has significant effects on atmospheric chemistry and dynamics: It triggers electron-induced reactions that lead to formation of free radicals in the atmosphere which further participate in catalytic ozone loss cycles [1]. Since ozone shields the Earth from harmful UV rays from the Sun, its depletion would lead to an increase in the biologically active UV radiation flux, with significant implication for human health, plants, marine ecosystems, and biogeochemical cycles [2]. While ionization of chlorine-containing anthropogenic molecules by solar UV radiation has long been recognized as an explanation for ozone depletion in the stratosphere, the role of cosmic rays and, in particular, low-energy cosmic electrons remain largely unexplained. These electrons interact with atmospheric gases of both natural and anthropogenic origin and can affect, thereby significantly the chemistry and dynamics of the ozone layer. Therefore, there is an urgent need to combine ground-breaking observations by modern satellite technologies and ground-based in situ/remote sensing with scientific expertise in biology, chemistry, environment, and radiation protection to study how such combined radiation fields can shape our natural habitat, affect the evolution of the biosphere, and impact our health status.

The European Partnership on Metrology project 21GRD02 BIOSPHERE (Metrology for Earth Biosphere: Cosmic rays, UV radiation and fragility of ozone shield at: www.euramet-biosphere.eu) aims to develop the necessary instrumentation, methods, and measurement infrastructure to assess how the increasing ionization of the atmosphere, caused by extraterrestrial radiation fields (cosmic rays and solar radiation) and amplified by anthropogenic emissions, affects the human and ecological health on our planet. To this end, measurement campaigns have been established to identify and quantify the relationship between cosmic rays, solar radiation, and anthropogenic emission, and to study their impact on the ozone shield. Thus, simultaneous modeling and traceable measurements of (i) ground-level muon and neutron fluxes, (ii) terrestrial and solar radiation, and (iii) the total ozone column (TOC) are required. Simultaneous measurements of cosmic rays (muons and neutrons), solar radiation, and ozone column were already performed at two European sites that provide the necessary infrastructure for accurate measurement of atmospheric profile parameters and have different anthropogenic emission inventories to account for their influence on ozone dynamics. The first measurement campaign was carried out from 1 June 2023 to 31 August 2023 at the National Centre of Scientific Research "Demokritos" (NCSR-DEM) station in Athens [3]. One measurement campaign at Milešovka mountain in Czech Republic (August to October 2024) has been completed, while another at the Meteorology Observatory of Lindenberg in Germany is being planned in 2025.

The second campaign took place in urban Brussels (Belgium) region (where two institutes involved in the project, BIRA-IASB and IRM-KMI, are located), from January 2024 to March 2024. This campaign involved numerous optical instrumentations (radiometers, spectrometers, pyranometers), amongst others from BIRA-IASB for accurate spectral and wavelength-integrated measurements of solar UV irradiance, giving access to UV-biologically effective dose rate (UV index) and atmospheric parameters (TOC and Aerosol Optical Depth—AOD). Noteworthy, BIRA-IASB managed the campaign. The Royal Meteorological Institute of Belgium (IRM-KMI) actively contributed with balloon soundings for vertical profiles of atmospheric parameters and ozone concentration and provided TOC, aerosol characteristics, and solar UV monitoring using ceilometer, aethalometer, nephelometer, and a Brewer spectrophotometer.

The simultaneous measurements of muon and neutron flux rates using new mobile detector systems from PTB, BFKH, and NPI were supplemented by data from the IRM-KMI, which also provided neutron flux monitoring. The monitoring data of aerosols and various molecules (traces species including anthropogenic contributions) are available from satellites and in situ measurements using BIRA-IASB instruments. In addition, different spacecraft provided the characteristics of the solar wind when it reached the Earth at 1 Astronomy Unit (AU) and the energetic electrons and protons trapped in the radiation belts using PROBA-V/EPT [4]. Some instruments take measurements permanently on the Spacepole Site of Brussels, and therefore also during the superstorm of May 2014 that occurred after the official campaign time.

In this work, we present the observations made during the campaign of Brussels and how solar activity affects space radiation. In the next section, we show that three kinds of solar events disturbed the terrestrial magnetosphere during the 3 months of measurements from January to March 2024: SEP, geomagnetic storms and an event on 24 March when both are combined. In section 3, we show with ozone profiles from 20 km to 100 km measured from space by Aura satellite that strong events can impact ozone mainly above 70 km. In section 4, we explain how, using AtRIS simulations, we have determined at which altitudes the different radiations (electromagnetic and particles) have their maximum ionization rate, depending on their energy. In section 5, we show that the very energetic electrons and protons observed in the radiation belts by the satellites PROBA-V and Joey Sat One Web are very affected by the geomagnetic storms and SEP, respectively. In section 6, we illustrate the cosmic rays Forbush decrease appearing during the event of 24 March 2024 using ground measurements of neutrons, muons, and other secondary cosmic rays. Moreover, Timepix3 observations enable us to determine the composition of the secondary cosmic rays. The Forbush decrease of 24 March is compared with the one of the Mother’s Day superstorm of 10–11 May 2025, since our ground-based monitors continued to measure even after March 2024. In section 7, we show the time evolution of UV observed from space including that observed during the May 2024 event. Section 8 shows how UV and total Ozone Content are correlated using measurements during the Brussels campaign. Specific peaks appeared on 11 May 2024, but they seem to be due to dynamic effects. Finally, in section 9, we discuss the health effects caused by exposure to space radiations (UV and energetic particles), before summarizing the major results in the conclusions.

2. Three large and different solar events

Different types of solar events (flares, Coronal Mass Ejections, SEP, for instance) generate different kinds of terrestrial perturbations, like injections of energetic protons and electrons, geomagnetic storms and modifications of electron density in the atmosphere for instance (e.g., [5] for a review). The first step is thus to identify the solar and geomagnetic activity during the period of interest.

The characteristics of the solar wind observed from 1 January 2024 to 31 March 2024 by OMNI (the multi-source data set of near-Earth solar wind's magnetic field and plasma parameters provided by NASA) are illustrated on Figure 1. Solar wind density (top), bulk velocity (2nd panel), proton temperature (3rd panel), pressure (4th panel), and Southward component of the Interplanetary Magnetic Field Bz (bottom panel) show that January was quiet in term of the solar wind. On 9 February, one observed the arrival of high velocity and high temperature particles, but they were not associated to a very high density, nor to negative Bz. That is why this SEP event did not generate a geomagnetic storm (see Figure 2), while it is also observed by GOES (Geostationary Operational Environmental Satellites) (see Figure 3).

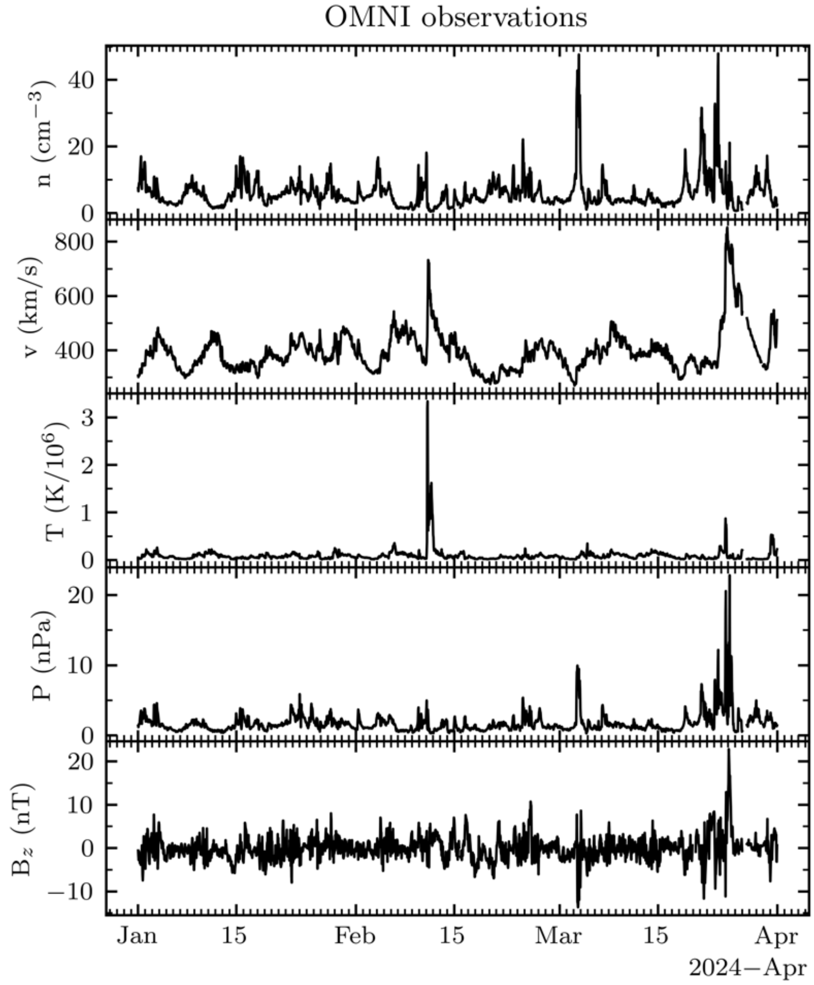

Figure 1. Solar wind density (top), bulk velocity (2nd panel), proton temperature (3rd panel), pressure (4th panel), and Southward component of the Interplanetary Magnetic Field Bz (bottom panel) from 1 January 2024 to 31 March 2024 observed by OMNI at 1 AU.

On 3 March 2023, there was a high peak of solar wind density, but it was not associated with energetic particles (not high velocity nor high temperature particles). Because the arrival of this high density event was associated to a southward direction of the interplanetary magnetic field (negative) Bz, as shown in the botton panel of Figure 1, the geomagnetic response was intense and a geomagnetic storm was generated with a planetary Bartels index Kp = 6 and Disturbed storm time index Dst < −100 nT (shown in the top and 2nd panels of Figure 2, respectively). A Dst < −50 nT is sufficient to indicate the presence of a geomagnetic storm. The A_p geomagnetic activity index (3rd panel of Figure 2) also shows strong activity at this date. The initial phase of the storm started at the arrival of the solar wind perturbation.

The most interesting event was the arrival of an interplanetary coronal mass ejection generating a geomagnetic storm on 24 March 2023. In Figure 1, all panels show that the event was due to the arrival of high-density energetic particles coming from the Sun, leading to an intense geomagnetic storm with Kp reaching 8 and a minimum of Dst ~ −125 nT on 24 March.

The 3-month period of the Brussels campaign is thus particularly interesting because it shows different kinds of solar events, leading to different effects in the space environment of the Earth.

The solar radio flux F10.7 at 10.7 cm is a solar activity index directly related to the number of sunspots and characterizing the electromagnetic emissions of the Sun. One can note an increase of this solar activity during the event of 24 March (see Figure 2 bottom panel) associated to the active region from which the solar eruption originated.

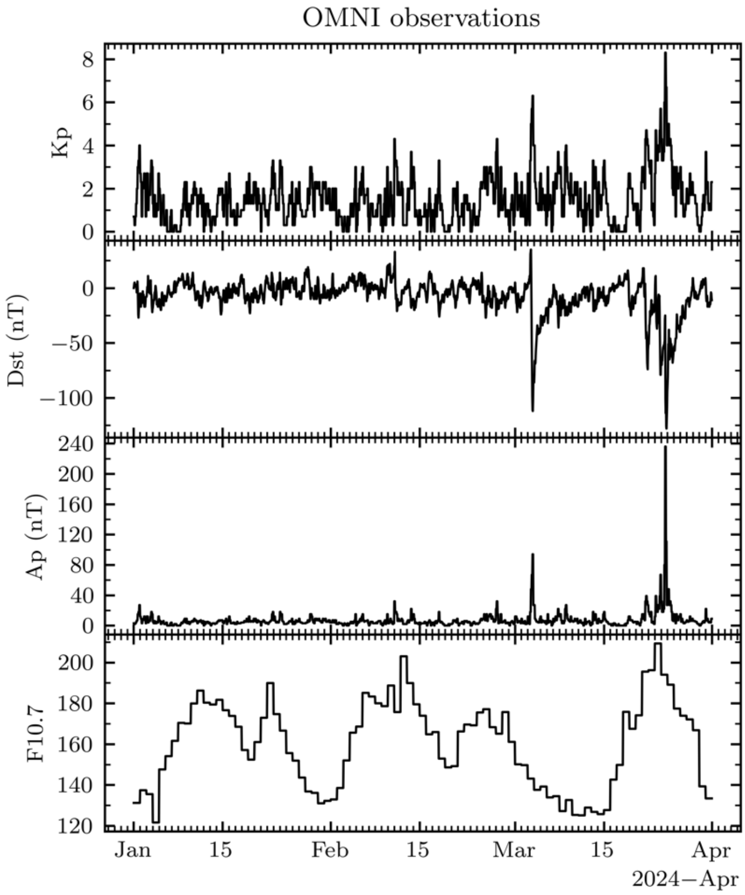

Figure 2. From 1 January 2024 to 31 March 2024, geomagnetic activity indices of Bartels Kp (top panel), Disturbed Storm time Dst in nanotesla (2nd panel), Ap index in nanotesla (3rd panel), and daily solar activity index F10.7 solar radio flux at 10.7 cm (bottom panel).

3. Ozone seen from space

During the period of 1 January to 31 March 2024, approaching the maximum of solar activity in the 11-year solar cycle, one can see in Figure 3 (2nd panel) that there were several energetic Solar Proton (SP) events observed by GOES measurements. Energetic protons are indeed detected by the GOES spacecraft revolving on a geostationary orbit at 6.6 Earth radii. The instrument Energetic Proton, Electron, and Alpha Detector (EPEAD) measures the integral flux of protons in 7 energy channels from 0.74 to 900 MeV.

Figure 3 (2nd panel) shows GOES measurements of proton integral fluxes: the fluxes > 10 MeV, > 30 MeV, and > 100 MeV respectively correspond to the blue, orange and green lines. The threshold of 10 cm^{-2} s^{-1} sr^{-1} for E > 10 MeV is generally used to qualify an eruption as a solar energetic particle event. Seven events reach this criterion during the measurement period, including the event on 24 March 2024. A comparison with Figure 1 shows that only the events with a flux E > 30 MeV (orange line) larger than 10 cm^{-2} s^{-1} sr^{-1} were detected as solar wind particles with velocity > 600 km/s with OMNI observations.

Ozone in Figure 3 (bottom panels) is measured using the Microwave Limb Sounder (MLS) that is part of the Earth Observing System (EOS) and was launched on the National Aeronautic and Space Administration (NASA) Aura satellite on 15 July 2004 [6]. Aura is in a near-polar 705 km altitude orbit with a daily global coverage of ~15 orbits per day. MLS observes thermal microwave emission from Earth's limb (the edge of the atmosphere) viewing forward along the Aura spacecraft flight direction, scanning its view from the ground to ~90 km every ~25 seconds [7].

MLS provides measurements of atmospheric components and properties. It measures ozone profiles in the atmosphere by measuring its emissions at 240 GHz. MLS provides daily ozone profiles with spatial resolution of 165 km × 3 km and a vertical resolution of 3 km to 6 km depending on the altitude. Here, we use the fifth version (v005) of Level 2 Ozone Mixing Ratio that provides an increase in the useable vertical range for scientific studies compared to the previous versions. In this version, ozone profiles range from 261 hPa to 0.001 hPa in 42 pressure levels. The daily zonal mean ozone profiles were computed at high latitudes in both hemispheres ([−82°, −60°] and [60°, 82°]).

The main ozone layer is in the stratosphere (10 km to 50 km). The second layer is well visible in the upper mesosphere and lower thermosphere (UMLT) between 85 km and 100 km, featuring strong seasonal variations, like the fainter tertiary layer around 75 km. These upper layers are mostly depleted during local summer due to increased photodissociation ([8] and references therein).

Some energetic proton events, indicated in Figure 3 (2nd panel) and by vertical solid black lines in all panels, coincide with some of the ozone concentrations in the mesosphere-thermosphere layers, and especially at altitudes around 90 km in the Northern hemisphere (see Figure 3, 3rd panel). This mesosphere-thermosphere ozone evolves naturally with local seasons, disappearing at the end of March while appearing in the Southern hemisphere (4th panel). On the contrary, the geomagnetic storms and substorms, indicated by vertical dotted black lines, do not show clear effect on ozone. Effects on the stratosphere are also not clearly observed during this period of time.

The observed effect of SEP on ozone can be explained by the fact that the precipitation of energetic particles into the atmosphere greatly disturbs the chemical composition from the lower thermosphere down to the upper stratosphere [1]. Most important are changes to the budget of atmospheric nitric oxides (NO_x = N, NO, NO_2) and to atmospheric reactive hydrogen oxides (HO_x =

H, OH, HO_2), which both contribute to ozone decrease in the stratosphere and mesosphere. Ozone losses are especially visible during periods of large geomagnetic activity and in Figure 3 in the Northern hemisphere (3rd panel) until 15 March due to the seasonal presence of mesospheric ozone. In the Southern hemisphere, the effects can only appear after 15 March when the mesospheric ozone is formed. Previous observations evidenced that geomagnetic activity may also impact the atmospheric dynamics down to the surface during polar winter and spring [1]. Energetic particle precipitation can also affect temperatures and dynamics of the atmosphere from the source region down to the stratosphere. A direct relation between ozone loss in the mesosphere and the arrival of solar energetic particles is observed during the big Mother's Day event of May 2024 [9].

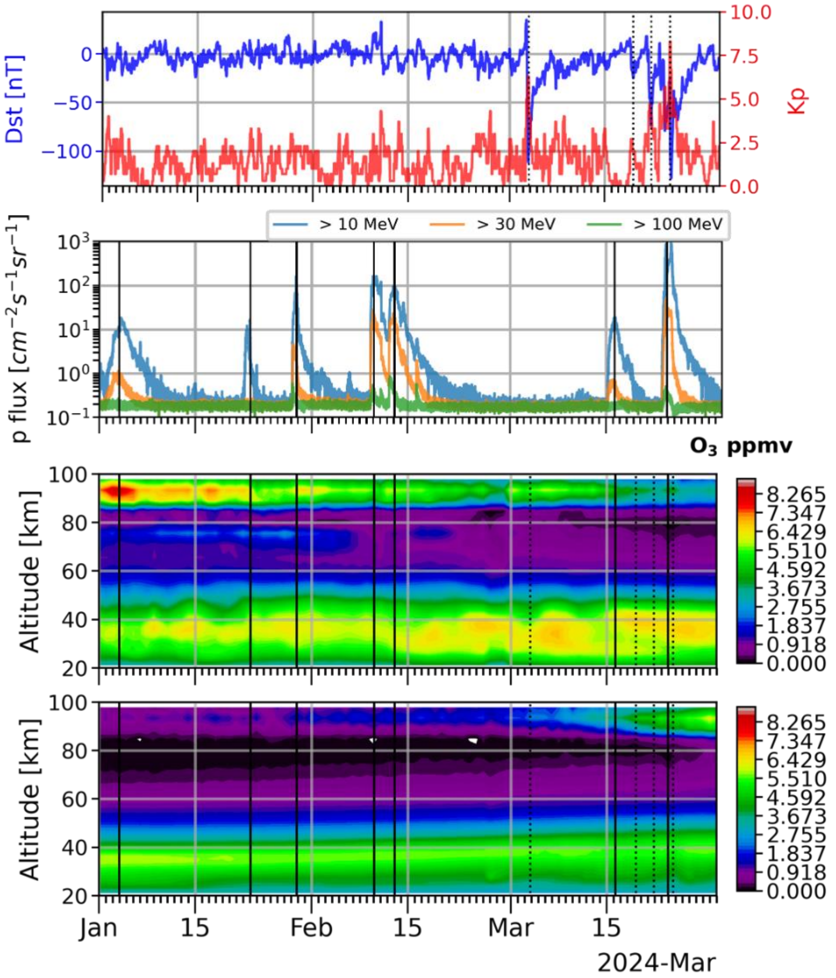

Figure 3. Observations from 1 January 2024 to 31 March 2024. Top panel: Disturbed Storm Time Dst and Bartels Kp geomagnetic activity indices, 2nd panel: GOES observations of integral proton fluxes with energy > 10 MeV (blue), > 30 MeV (orange) and > 100 MeV (green) at the geostationary orbit (6.6 Re). Bottom panels: In the North hemisphere (3rd panel), and in the South hemisphere (bottom panel), concentration of ozone in part per million by volume (ppmv) as observed by MLS/Aura as a function of the altitude from 20 km to 100 km.

4. The different sources of ionization

Model studies can help us to better understand the influence of particle precipitation on the Earth's atmosphere. Different sources can ionize the atmosphere, as illustrated on Figure 4 showing the maximum (solid lines) and minimum (dashed lines) ionization rate of different processes as a function of the altitude. The ionization rates illustrated in Figure 4 are obtained using AtRIS (Atmospheric Radiation Interaction Simulator), a Geant4 Monte Carlo code used to simulate the effects of energetic particles on the atmosphere [10]. The energy range of the injected particles used in the simulations is indicated in Figure 4 next to each ionization source. The assumptions made in the AtRIS simulations are similar as in [11]. The ionization of by UV and X rays comes from the IRI (International Reference Ionosphere) model [12].

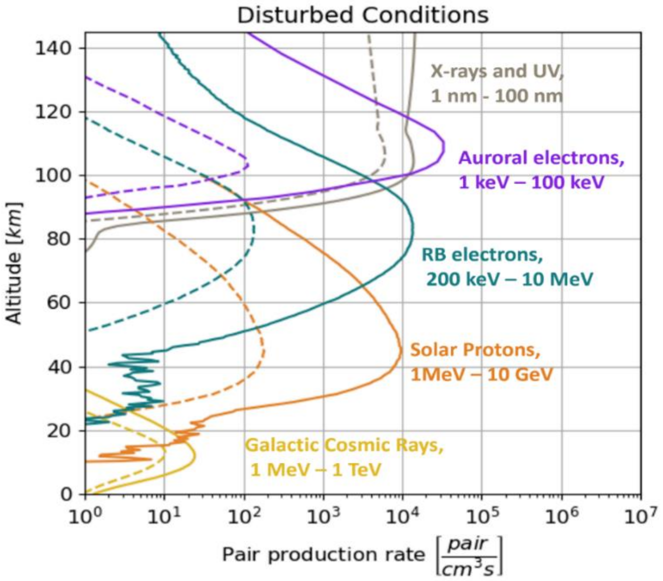

Figure 4. Ionization rate obtained with AtRIS (maximum in solid lines and minimum in dashed lines) as a function of the altitude due to different processes [5].

The main source of atmospheric ionization is not due to particles, but to the solar ultraviolet and X radiations that create the ionosphere at high altitudes, with a maximum of ionization around 250–300 km. The ionization rate in the ionosphere is maximum during the day and maximum solar activity. The ionization rates due to UV and X rays are illustrated by the grey lines in Figure 4.

Another source of ionization is the precipitation of particles with a wide energy range. Such injections take place mainly at lower altitudes and are constituted of auroral electron precipitation (in purple in Figure 4), more energetic electrons from the radiation belts (RB in dark green), sporadic solar energetic particle events (solar protons in orange), and highly energetic galactic cosmic rays (GCR, in yellow in Figure 4). The most energetic particles, i.e., the GCRs, the lower the altitudes they reach. The different sources are modulated by the solar position (day/night asymmetry mainly for solar UV), by the latitude (magnetic field screens low latitudes from ionization and radiation dose by energetic particles), and by the solar activity (anti-correlation for GCR at low altitude and direct correlation for the solar wind mainly in the high-altitude ionosphere).

GCR is a continuous source of ionization, UV and X rays are present during day-time, and the other sources are associated with sporadic events. During quiet time, the ionization is due to UV and X rays at high altitude and galactic cosmic rays at low altitude.

Due to the geomagnetic field shielding that prevents particles from reaching the atmosphere at low latitudes, the ionization due to injections of particles appears mainly at high latitudes. A magnetic cutoff is present for all particle sources, contrary to the electromagnetic sources like UV and X rays. At the equator, the ionization is almost only due to solar UV/X and is maximum when the Sun is highest above horizon.

The galactic cosmic rays form a continuous source of radiation that constantly ionizes the Earth’s atmosphere with a maximum rate appearing around 15 km (named the Pfotzer maximum). The ionization rate is maximum during minimum solar activity due to solar magnetic field modulation. Only the most energetic particles of the galactic cosmic rays can penetrate at low altitudes, mainly in polar regions due to the cutoff of the terrestrial magnetic field at low latitudes. While geomagnetic storms result in injections of additional particles (mainly electrons) in the atmosphere that can increase ionization during short period, CMEs can result in a longer decrease of the ionization during several days due to changes in recombination rates of the ions and electrons, decrease of cosmic rays, and reduction of the plasmasphere [13].

These modifications can also alter the composition of the atmosphere and especially the ozone that plays an important role in the filtration of the solar UV radiation and protecting life at the surface of the Earth. From Figure 4, one can see that the mesosphere can be affected by injection of energetic electrons from aurora above 100 km and around 80 km by electrons from the more energetic radiation belts mainly during geomagnetic storms. Energetic electron precipitations have indeed been found to have a significant influence on ozone in the mesosphere between 60 km and 80 km, with short-term depletions reaching 90% [14]. At lower altitudes of the stratosphere, solar energetic protons can cause ionization. Below 20 km, only the cosmic rays have enough energy to penetrate.

The energetic particles precipitating into the atmosphere mostly interact with N_2 and O_2 but also with the less abundant trace gases. They initiate reactions where the most important are excitation, dissociation and ionization. The secondary electrons produced in ionization undergo further collisions and after slowing down to low energies they can form negative ions, e.g., via dissociative electron attachment reactions with molecules or they directly bind to molecules via three-body collisions. Therefore, negative ions are formed alongside to positive ions, which both influence the upper atmospheric chemistry. The presently used standard chemistry-climate models consider the most important primary reactions. In order to enable future more accurate modeling, we will provide a collection of accurate atmospheric collision rates and cross sections in an open data base. The data are collected from literature or measured in lab-based experiments [15].

5. Radiation belt effects

5.1. Observations of PROBA-V/EPT

The Energetic Particle Telescope (EPT) measures the fluxes of high-energy particles in the radiation belts and the injection of solar protons in the magnetosphere [4]. This instrument was developed by the Center for Space Radiation (CSR) at UCLouvain in Belgium, with the collaboration of the Royal Belgian Institute for Space Aeronomy and QinetiQ Space (presently Redwire Space). This detector has been launched on 7 May 2013 onboard the ESA (European Space Agency) satellite PROBA-V. The spacecraft was sent to a sun-synchronous polar Low Earth Orbit (LEO) orbit at an altitude of 820 km, with an inclination of 98.73° and a descending node at 10:30 am local time. The concept of the EPT is based on the relationship between the stopping power of a material and the energy of incident charged particles [16]. The EPT was designed for real-time and contamination-free measurements of charged particle spectra in the space environment, and is able to discriminate between electrons, protons, alpha particles and heavier ions while performing direct measurements of their energy spectra. The EPT features two energy sections. The Low Energy Section (LES) measures only lower energy electron fluxes, while the High Energy Section (HES) measures electron, proton, and heavier particle fluxes of higher energy. The EPT measures differential flux of electrons above 500 keV in 6 energy channels, and of protons above 9.5 MeV in 10 energy channels.

5.2. Energetic electrons

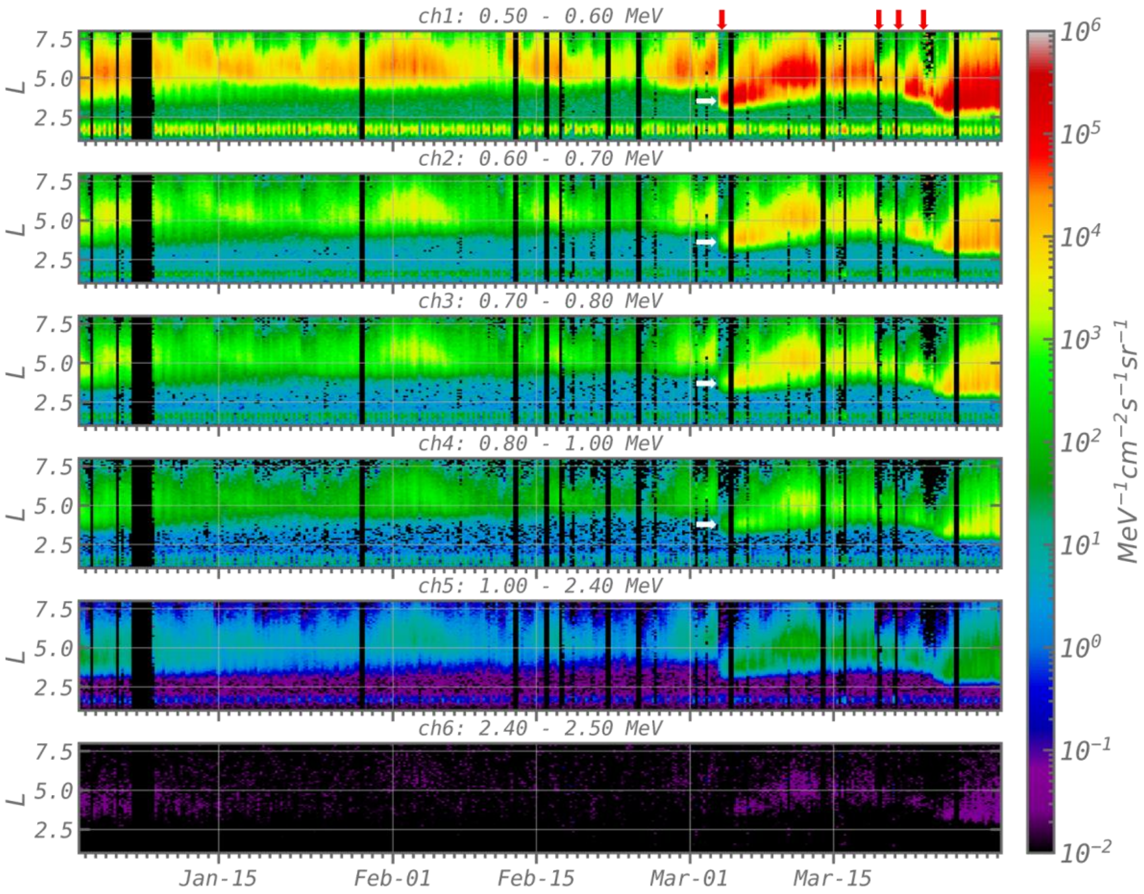

Figure 5. Electron fluxes observed from 1 January to 31 March 2024 as a function of the McIlwain parameter L (vertical axis in Earth's radii) and time (horizontal axis) for the 6 energy channels of EPT on board PROBA-V using the same color scale. The red arrows indicate the dropouts, while the white arrows indicate the injections of the first storm of Mars 2024.

Figure 5 shows the time evolution of the electron fluxes as a function of the McIlwain parameter [17] corresponding to the radial distance of the intersection of the field line with the magnetic equator. A clear dropout [18] appears in the outer belt at the beginning of the two geomagnetic storms of March 2024 (see red arrows in Figure 5 for each dropout associated even to small events), followed by injections of electrons (white arrows for the first geomagnetic storm of Mars, at all energy ranges) at low L values in the slot, but not in the inner belt at L < 2.5. Smaller dropouts are also visible at each small Dst event (see Figure 2). Such dropouts and flux injections in the slot are regularly observed during the geomagnetic storms [19] and their depths have been shown to be directly correlated to the value of Dst [18]. After the flux injection at the beginning of March, the slot slightly increases with an inner edge of the outer belt slightly moving to higher L values for all energies during the following days later until new injections appear due to the next storm. The physical mechanisms leading to the flux variations have successfully been simulated considering magnetopause shadowing and radial diffusion to explain the major characteristics of outer radiation belt electron dropouts and flux increase during the storms, and diffusion coefficients of wave-particle interactions for the gradual scattering that depopulates the slot region and the outer belt after storms [20]. The positions of the inner and outer belts are strongly related to the energy of the particles and on the position of the plasmapause and the auroral oval [21]. Moreover, the electron fluxes of the radiation belts are also influenced by human activities, since the very low-frequency transmitter in the Northwest Cape of Australia has been observed to pitch-angle scatter electrons with energies from 30–800 keV, modifying the fluxes measured by LEO satellites [22].

Such energetic electron flux variations directly due to the geomagnetic activity are problematic for space missions, especially for astronauts, electronic devices, and solar panels. That is why Machine Learning models have been developed (e.g., [23]) to predict these flux variations during space weather events.

5.3. Energetic protons

Contrary to the electrons, the protons are not correlated to the geomagnetic storms (Dst) but to the arrival of SEP [24]. The solar protons detected by GOES at the geostationary orbit (see Figure 3 panel 2) are also detected by PROBA-V/EPT at 820 km, as shown Figure 6. The proton differential fluxes observed by EPT from 9.5 MeV to 155 MeV on board the satellite PROBA-V are averaged in L and time bins (L bins 0.25 Time bins: 1 h). EPT shows the same injections of energetic protons as GOES, in January 2024 limited to energies < 29 MeV, while in February 2024 and on 23 and 24 March 2024, the fluxes reach E > 61 MeV. The flux goes down to L < 4, but no protons are injected in the continuously trapped proton belt visible at L < 2.5. This inner proton belt corresponds to the South Atlantic Anomaly (SAA) at these low altitudes, and it is only slightly modulated by the solar cycle [25]. EPT showed its first injection of protons in the South part of the SAA during the 11 May 2024 Mother’s Day event, the strongest Dst event for the last 20 years, as well as the unusual development of multiple electron belts during more than one month after this event [26].

5.4. Characterization of space radiation in LEO at 600 km

The spectral and composition characterization of the space radiation field in LEO at 600 km is measured by a Timepix3 detector [27] onboard the JoeySat OneWeb satellite. The Timepix detector is implemented as a miniaturized high-resolution radiation monitor for spacecraft. The pixel detector provides the composition and spectral characterization of the ionizing radiation field along the satellite orbit. The decomposition into the radiation components is given as detailed particle flux plots over time in Figure 7.

The data show intervals of onset (23 March) and decline (24 March) of geomagnetic-solar activity. Correlations are observed for the proton component (Figure 7b) and, with delay, also the low-energy and X ray component (Figure 7d). The particle fluxes produced are omnidirectional (over the full field-of-view of the detector) and integrated over all particle energies (for protons above 35 MeV). Electrons are registered above few MeV (Figure 7c) and, as secondary low-energy electrons below approximately 1 MeV (Figure 7d). A narrow low-energy (tens to few hundred keV) gamma ray component is also registered as one group together with the high-energy electron component (Figure 7c).

Figure 6. Proton flux measured from 1 January 2024 to 31 March 2024 by PROBA-V/EPT in 6 energy channels.

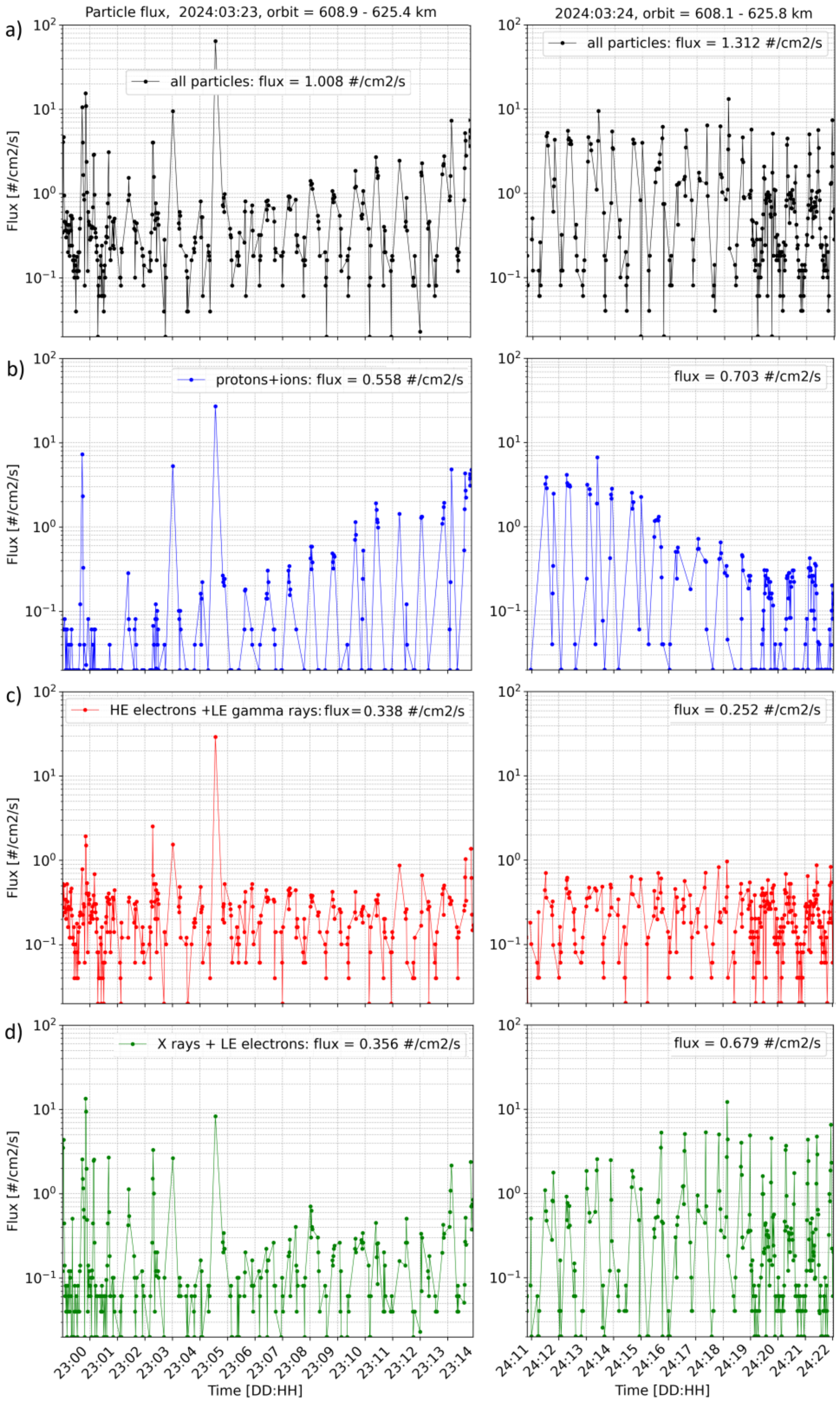

Figure 7. Particle flux (displayed in log scale) of space radiation measured by Timepix3 in LEO orbit at 600 km onboard the JoeySat OneWeb satellite: a) All particles, b) protons, c) electrons and low-energy gamma rays, and d) X rays. Data is given for a 14-hour interval on 23 March 2024 (left) and an 11-hour interval on 24 March (right) 2024.

The data provides direct information on the radiation components and their variance along the satellite orbit and over extended periods of time. The radiation field and resolved components are registered in limited energy range as follows: Protons above 40 MeV, electrons above 3 MeV, low-energy gamma rays, and X rays in the region ≈ 3–50 keV. The gamma rays are detected with decreasing detection efficiency. Ions of energy above ≈ 50 MeV/u are registered together with the protons. The spectral response is determined and limited by the semiconductor sensor of the pixel detector (silicon 500 µm thick) and the shielding (Al 5 mm thick) mounted on top of the Timepix3 detector in JoeySat.

The space radiation field is continuously evaluated along the satellite orbit of detailed particle fluxes and dose rates as time histories at the minute scale. For the charged particle components, protons and electrons, can be produced detailed angular fluxes (in few broad angular bins) as well as detailed deposited energy spectra and linear energy transfer (LET) distributions integrated over longer data intervals.

6. Measurements of Secondary Cosmic Rays on the Ground

6.1. Neutron monitors

During solar energetic particle events, high-energy protons with sufficient rigidity can penetrate the Earth’s upper atmosphere and interact with neutral atmospheric atoms to produce secondary particles, including neutrons. These neutrons are detected by ground-based neutron monitors. Solar particle events (SEPs) are often associated with Coronal Mass Ejections (CMEs), as the shock waves produced by CMEs can accelerate particles to high energies. Conversely, CMEs are also frequently accompanied by SEPs when particle acceleration occurs. CMEs can also lead to a temporary decrease in the count rates of ground-based neutron monitors—a phenomenon known as a “Forbush decrease” (FD) (e.g. [28]). A clear FD is observed on 24 March 2024, illustrated in Figure 8 by the sharp decrease coinciding with the arrival of the magnetic cloud in the CME. FDs, i.e., short-term drops in the flux of galactic cosmic rays, are caused by the shielding from strong or turbulent magnetic structures in the solar wind, especially CMEs and their associated shocks. In Figure 8, the observations at each station have been separated in different lines, with the 0 corresponding to each curve on the dotted line.

The maximum amplitude of the FD (see last column of Table 1) is primarily influenced by the geomagnetic latitude of the station (5th column). Table 1 lists neutron monitor stations in order of increasing latitude. Variations in the FD, however, can also arise due to other factors, such as the type of instrument used and the local geomagnetic environment during the storm. In Athens, which is at a relatively low latitude, the effects of solar and cosmic particles are less pronounced, complicating the detection of such events during the first measurement campaign. However, this location provides better opportunities to observe other phenomena, such as aerosol, temperature, and water profiles [3].

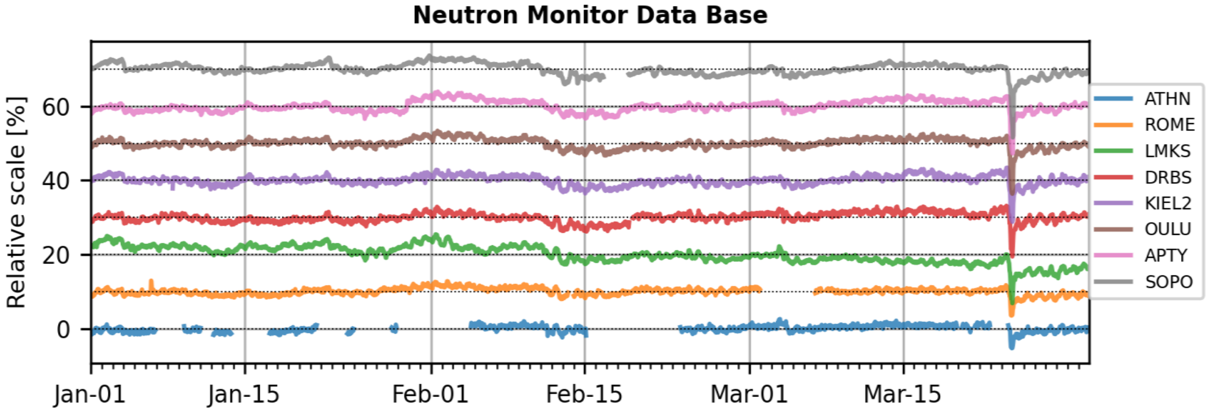

Figure 8. Observations of neutron monitor stations located at different latitudes summarized in Table 1. The perturbation on 24 March 2024 is well visible. The neutrons show a Forbush decrease during the storm due to the higher protection of the terrestrial magnetic field from the galactic cosmic rays.

Table 1. Characteristics of the stations where neutron monitors are located with increasing latitude, including altitude, full range of Vertical Rigidity Cutoffs (Rc) and maximum Forbush decrease during the 23 March 2024 event.

Full Name	Short Name	Alt (m)	Rc (GV)	Coords (lat, lon)	Max FD
Athens	ATHN	260	8.53	37.97, 23.78	−5.28%
Rome	ROME	0	6.27	41.86, 12.47	−6.47%
Lomnicky	LMKS	2634	3.84	49.20, 20.22	−13.14%
Dourbes	DRBS	225	3.18	50.0971, 4.59003	−10.52%
Kiel	KIEL	54	2.36	54.3399, 10.1199	−11.20%
Oulu	OULU	15	0.81	65.0544, 25.4681	−13.59%
Apatity	APTY	181	0.65	67.5704, 33.3935	−12.70%
South Pole	SOPO	2820	0.1	−90.000, 0.00000	−18.39%

6.2. Muon monitors

Muons were detected during the Brussels campaign with the PTB’s mobile position-sensitive muon detector DECOS2 (see Figure 9), new version of the PTB reference detector DECOS1 [29]. DECOS2 consists of two units, each with a 2-dimensional spatially sensitive readout. The units can be rotated in space and their separation can be adjusted. Each unit contains two crossed layers, each composed of ten EJ-200 plastic scintillators bars (50 cm long, 5 cm wide and 1 cm thick). This arrangement of scintillator bars, in combination with quadruple coincidence detection (one for each scintillator layer), enables position-sensitive detection with a pixel size of 5 cm × 5 cm. The variable distance between the two detector units allows for an adjustable field-of-view (FOV) of the detector. DECOS2 has been successfully used in two measurement campaigns in Athens and Brussels, each fixed for a period of three months, to count cosmic muons at two altitudes, latitudes, and under varying atmospheric conditions. The vertical profiles of atmospheric parameters (temperature, density, and aerosols) at the measurement sites in Athens and Brussels were obtained using LIDARs (Light Detection and Ranging) and Radiosondes. These data were then used as input for Monte Carlo (MC) simulations to investigate the correlation of primary cosmic rays (PCR) with secondary cosmic rays (SCR) measured on the ground and at different altitudes. MC simulations predict a negative correlation of the atmospheric pressure with the muon flux at altitudes below about 12 km and a positive correlation at higher altitudes. Panels a and b in Figure 9 show the anti-correlation of the pressure with the SCR count rate in the pressure-uncorrected data for both muons (measured during the measurement campaign at the urban Space Pole site in Brussels) and neutrons measured at the Belgian neutron monitoring station in Dourbes. In both cases, the FD can be seen as a small signal drop embedded in large pressure-dependent fluctuations. In addition to these fluctuations, a weak anti-correlation between secondary cosmic count rates and temperatures is also observed. The barometric coefficient (β) obtained from the data is about -0.19% hPa^{-1}, while the ground temperature coefficient (α_T) is about -0.01% $°C^{-1}$. Further investigations into the influence of the vertical temperature profile are being conducted.

The pressure-corrected muon and neutron data in Figure 9 [panels c) and d)] show the FD event on 24 March 2024 due to the solar energetic particle (proton) event followed by a geomagnetic storm. The solar event enhances the magnetic shielding, leading to a temporary reduction in the flux of galactic cosmic rays and hence, a decrease in the cosmic rays reaching the Earth. In the muon data, [panel c)] a signal decrease of (7 ± 3) % is observed, which is about 30% smaller than the count rate decrease in the neutron monitor (about 10%, see Table 1). This difference in the magnitude of the FD stems from the fact that the bulk of the muon signal is produced by higher energy PCRs (typically above few GeV), which are less affected by this magnetic field modulation. Neutrons observed on the ground, on the other hand, which are products of both lower and higher energy PCRs, show a more pronounced FD due to the stronger magnetic deflection of low energy PCRs.

The BIOSPHERE team has also access to measurements of the SEVAN detector installed on Milešovka mountain (altitude: 840 m, latitude: 50.55°) in Czech Republic. The SEVAN detector [30,31] was designed to detect high energy particles, mainly from secondary cosmic rays. It consists of three active plastic detectors coupled with photomultiplier tubes and separated by lead. Top channel has an active volume of $100 \times 100 \times 5$ cm^3, middle has $50 \times 50 \times 25$ cm^3, and the lower has the same setup as the top one. There are two 5 cm layers of lead that separate particles by their type and energy. If a photon or electron has lower energy, it will trigger only the top channel and thus shows the coincidence of "100". Neutrons will not trigger the top channel and by interacting with the top lead layer, they will trigger a signal in the middle channel that is thick enough, hence the coincidence of "010". Muons, on the other hand, trigger signals in all channels they pass and are thus the main part of the coincidence "111&101".

Figure 10 shows 10 minutes averages of SEVAN measurements from 24 to 25 March 2024. The muons generated by cosmic rays are disturbed by the storm, in a way very similar to the neutrons. The muons are illustrated Figure 10 (bottom panel) with SEVAN observations, together with neutrons (panel 2) and low energy particles (top panel). All show the FD followed by several bumps that are especially visible for the muons with a daily cycle.

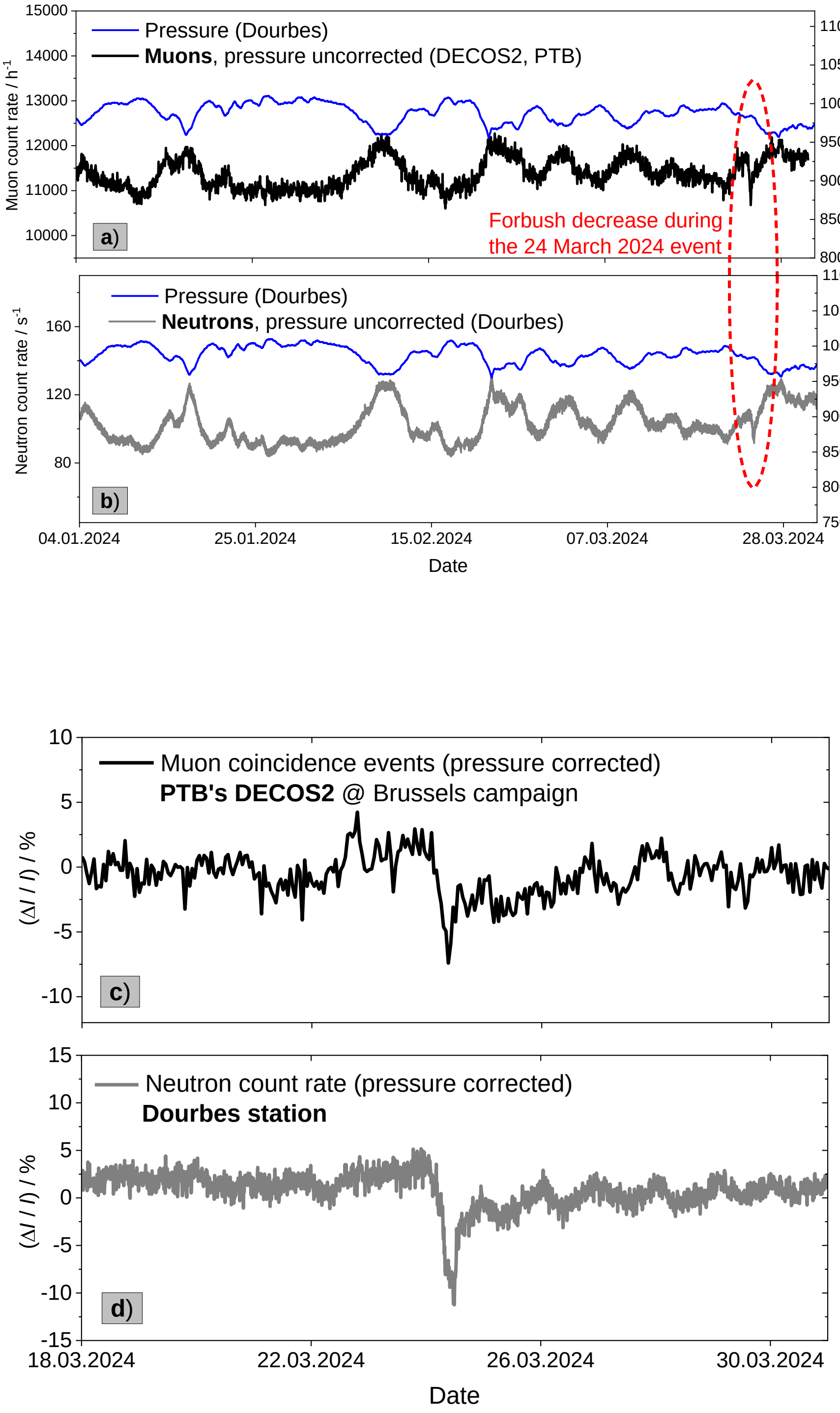

Figure 9. a) Anti-correlation between cosmic muon flux measured at the urban Space Pole site in Brussels and ground atmospheric pressure. b) Anti-correlation between neutron count rates measured at the Dourbes neutron monitor and ground atmospheric pressure. Pressure-corrected and normalized c) muon coincidences (1 h averages) and d) neutron count rates showing the FD event on 24 March 2024.

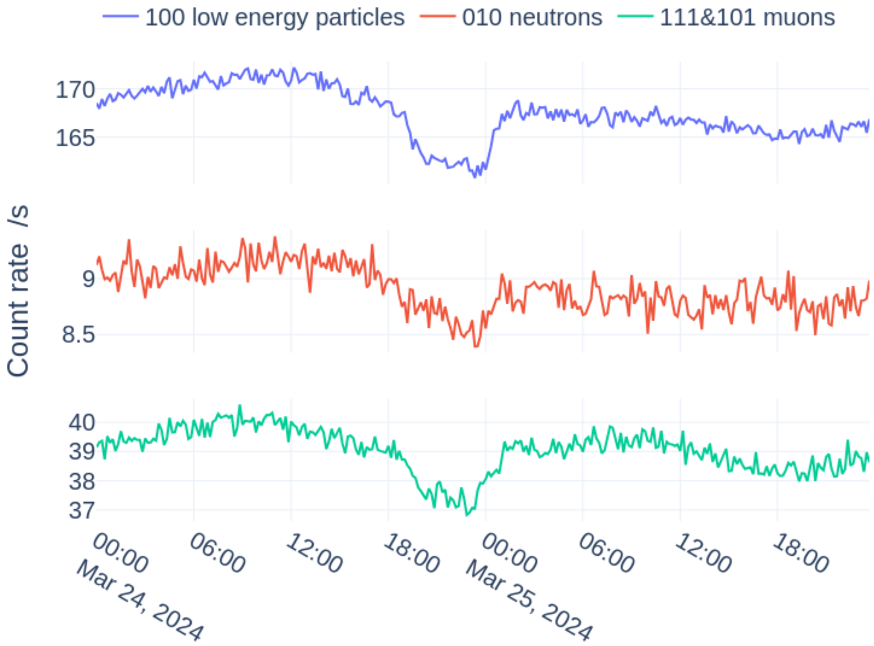

Figure 10. SEVAN measurements of the Forbush decrease observed on 24 March 2024 for secondary cosmic rays (top panel in blue), neutrons (middle panel in red), and muons (bottom panel in green).

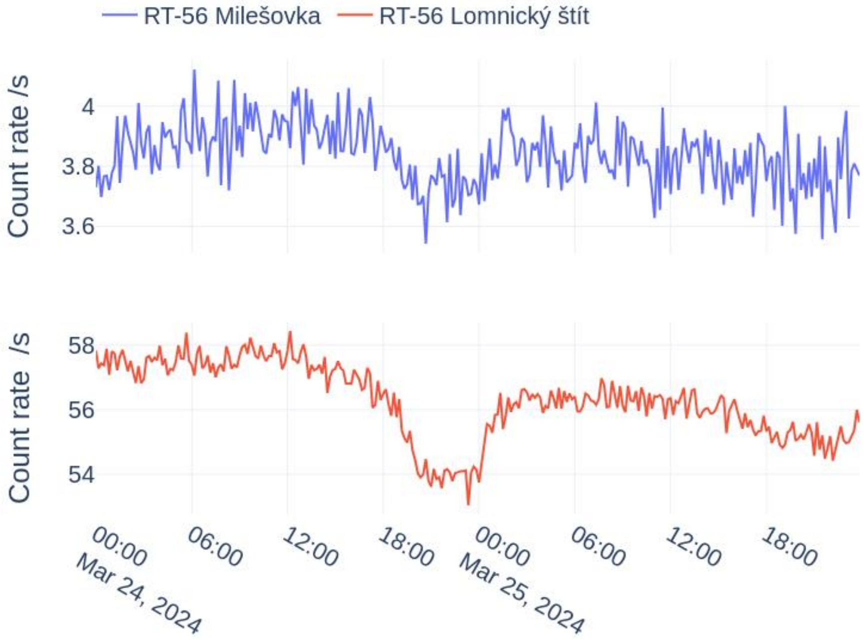

Figure 11. Measurements of the large gamma spectrometers on Milešovka, Czech Rep. (top panel in blue) and in Lomnický štít on the Tatras mountains, Slovakia (bottom panel in red) on 24 and 25 March 2024 (10 minutes averages of pressure uncorrected count rates).

Figure 11 shows particles with deposited energies over 3 MeV measured by the gamma-ray spectrometers on Milešovka, Czech Rep, and Lomnický štít, Slovakia. Lomnický štít's altitude is 2634 m and has a geomagnetic vertical cut-off rigidity of 4 GV. The sensitive area in Lomnicky stit is a 10 × 10 × 40 cm^3 large NaI(Tl) crystal. On Milešovka, it is the same gamma spectrometer system as on Lomnický štít, but with 3 × 3 BGO crystal instead of NaI (Tl). Spectrometer data 10 minutes averages of pressure uncorrected count rates. The FD is also well visible.

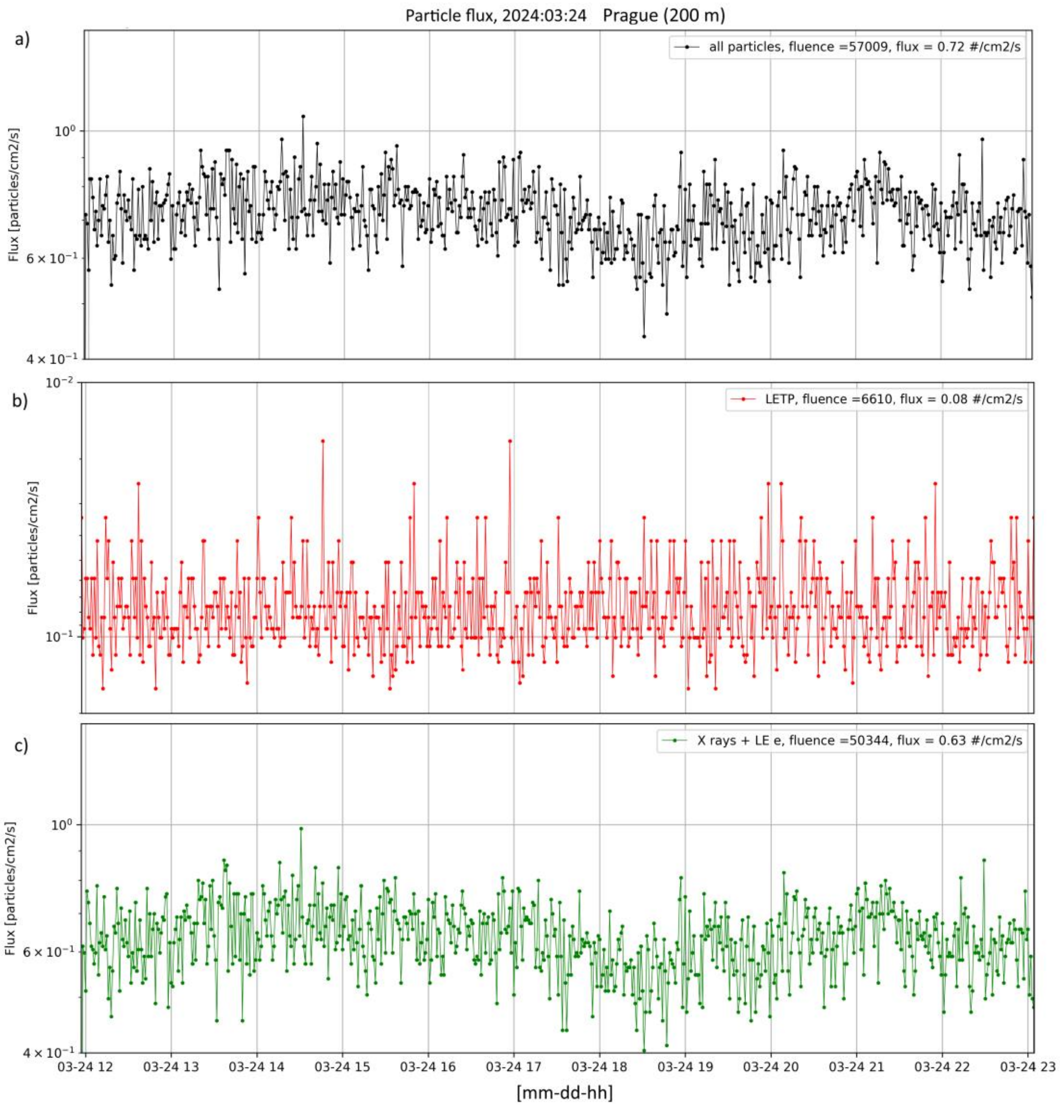

Figure 12. Omnidirectional particle flux of SCR measured in Prague (200 m altitude) by Timepix3 with a 500 mm thick silicon sensor. Data shown for (a) all particles, (b) light charged particles (electrons and muons), and (c) X rays. The results are given for a 11 h period on 24 March 2024 (UTC times shown).

6.3. *Composition of secondary cosmic rays*

Information on the composition and spectral characterization of secondary cosmic rays at the ground level were complementary performed with semiconductor pixel detectors Timepix3.

Measurements were performed with miniaturized stack Timepix3 telescopes [32], which operate at room temperature and are controlled by standard computer. The device comprises two MiniPIX Timepix3 cameras equipped with silicon sensors of different thickness (300 and µm) assembled in a close stack configuration with a 10 mm spacing gap between the pixel detectors. The Timepix3 detectors operate in sync and are readout in continuous data driven mode with minimal deadtime.

Measurements of SCRs on the ground level were carried out in Prague, at 200 m altitude, during March 2024. Figure 12 shows the measured particle flux for all particles and for the selected heavy charged particle component (protons, neutrons) and light charged particle (electrons, muons) component.

The whole radiation field measured by the detector [33] (given also in Figure 12) consists primarily of all charged particles, both light e.g., electrons and heavy e.g., protons, as well as photons (X rays and low-energy gamma rays) in limited energy range (around 5–50 keV) registered with limited (decreasing) detection efficiency. In the data shown Figure 12, a limited variation with the FD is apparent starting after around 18 h. Higher sensitivity will be provided by evaluation of synchronized data in the pixel telescopes.

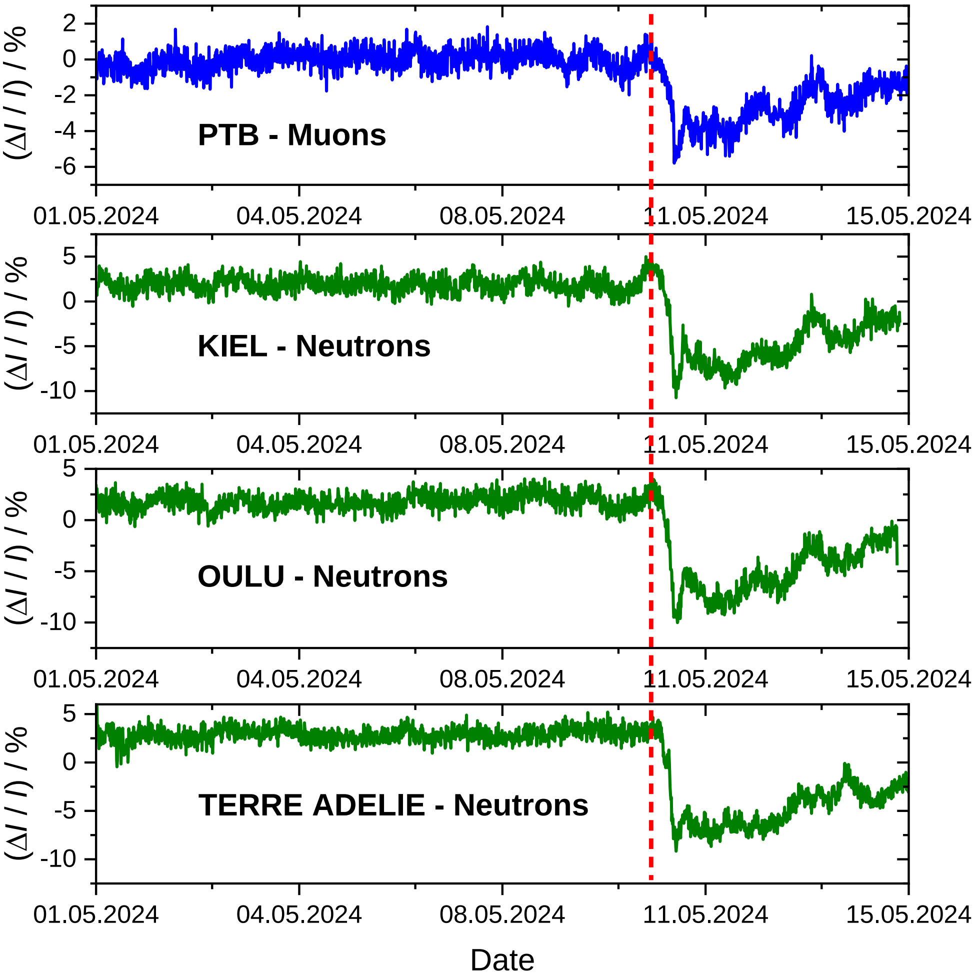

Figure 13. The Forbush decrease event on 11 May 2024 (the so-called “Mother’s Day solar storm”), measured with PTB’s reference muon detector DECOS1 (top panel in blue), and by different neutron monitors in Kiel, Oulu, and Terre Adélie (other panels).

6.4. Forbush decrease on Mother's Day on 11 May 2024

As we mention the Mother's Day extreme event, it is interesting to compare the Forbush event of 24 March 2024 with that of 11 May 2024, especially for the instruments involved in the Biosphere campaign measured in May 2024. Many articles have been, and are being, written for this event because this is the strongest storm for the last 20 years and it caused very unusual effects in the terrestrial environment like auroras at lower latitudes [34], ionization variations in the ionosphere (e.g., [35]) and in the plasmasphere [36], temperature changes in the mesosphere and thermosphere [37], ozone changes as seen using Aura/MLS observations [9], and injections in the radiation belts using PROBA-V/EPT data [26]. Neutron monitor data have not been greatly reported.

Figure 13 illustrates muons (top) and neutrons (other panels) count rates from 1 May 2024 to 15 May 2024 in different stations. The characteristics of Kiel and Oulu are given in Table 1. PTB (Braunschweig) is at a latitude (North) of 52.27° (altitude ~80 m) while Terre Adélie is in the South hemisphere at a latitude of −66.65° (altitude 32 m).

The muon signal starts to decrease in the afternoon of 10 May 2024 reaching a maximum decrease of (5.8 ± 1) % at about 11 pm (UTC). The pressure-corrected muon signal also shows a slight increase in muon precipitation during the day and a decrease during the night (day-night asymmetry). On 10 May, all detectors recorded a sharp decrease in the count rate, with the neutron count rate decreasing over 40% more than the muon count rate, much higher than the maximum decrease measured in March 2024 and summarized in Table 1. One can note also a ground level enhancement, i.e., the small bump just after the decrease in all panels of Figure 13, associated with the arrival of very energetic proton fluxes [26].

7. UV Observations in space

Figure 14 shows the variability of the UV Solar Spectral Irradiance (SSI) with time from 1 January 2024 (day 0) to 31 May 2024 (day 152) and with the wavelength between 200 nm and 400 nm (measured outside the atmosphere by the prism spectrometer SIM on TSIS-1 on board the International Space Station (ISS) [38]. The SSI is much more variable for short wavelength and almost negligible above 290 nm. Evidently, the periodicity of 27 days corresponding to the solar rotation, due to the asymmetric repartition of the active regions at the surface of the Sun, further implies a modulation of the SSI UV with the solar rotation.

This periodicity is also visible in Figure 15 on other proxies of the solar activity like the sunspot number (top panel), the radio flux at 10.7 cm (middle panel), and the Lyman-Alpha flux at 121 nm (bottom panel). While the correlation between these proxies is obvious, the position of their maximum is not the same, especially in May 2024 (9 May for F10.7, 13 May for sunspot number, and 16 May for Ly-alpha). The SSI peak of May 2024 appears a few days after the Mother's Day superstorm of 11 May 2024 that influenced the space environment of the Earth in many ways [26].

The index MgII related to the depth of MgII around 280 nm [39] is another proxy with this periodicity associated to the solar activity in the chromosphere that can be used to model the SSI variability SSI between 120 nm and 400 nm and is illustrated in Figure 14 (bottom panel) from 1 April 2024. One can see that the maximum is around 15 May 2024.

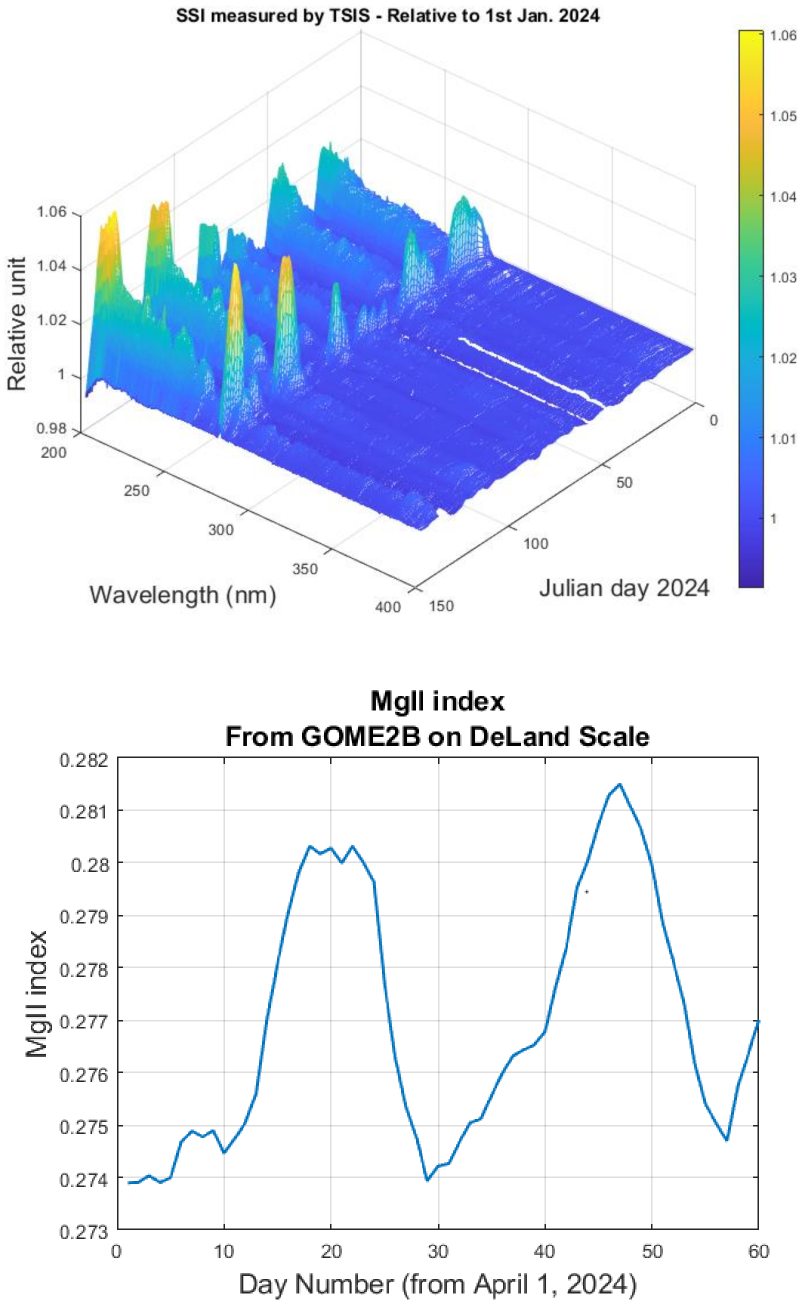

Figure 14. Upper panel: Solar Spectral Irradiance (SSI) relative to 1 January 2024 measured outside the atmosphere by the prism spectrometer SIM on TSIS-1 on board the International Space Station (ISS) from 1 January 2024 to end May 2024 for wavelength between 200 nm and 400 nm. Bottom panel: MgII index (rescaled from GOME2B), as measured from 1 April to 21 May 2024.

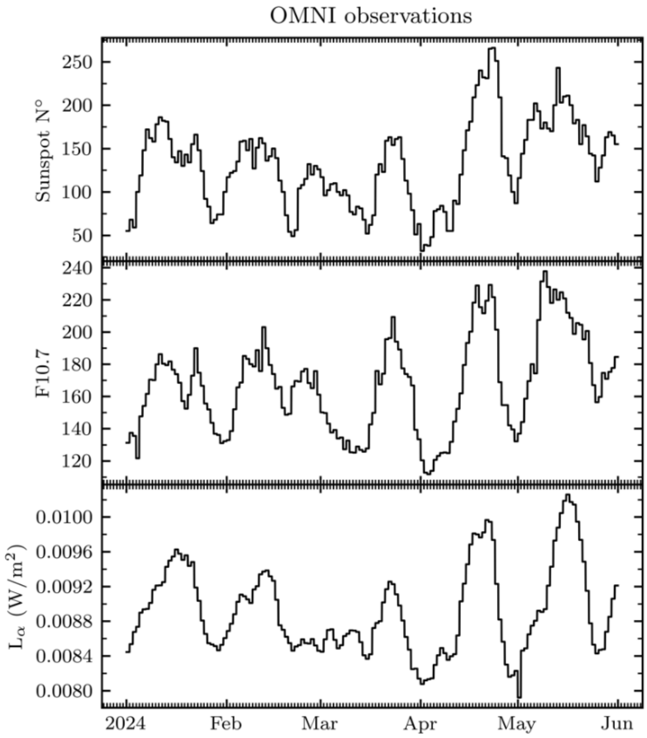

Figure 15. Indices of the solar activity measured from 1 January 2024 to 31 May 2024: The sunspot number (top panel), the radio flux at 10.7 cm (middle panel), and the flux at 121 nm Lyman-Alpha (bottom panel).

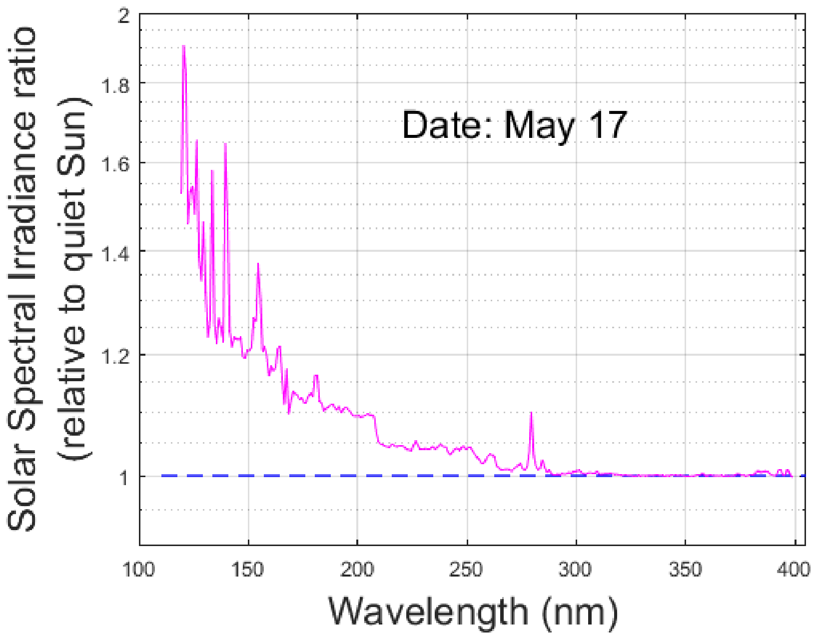

Figure 16. The ratio between the Solar Spectral Irradiance (SSI) relative to 17 May 2024 measured outside the atmosphere by the spectrometer SIM on TSIS-1 on board the ISS and a quiet Sun reference spectrum. The figure shows the UV SSI variability as a function of wavelength between 110 nm and 400 nm.

Figure 16 illustrates the wavelength dependence of the UV SSI variability, which reaches 100% at Lyman-alpha and around 10% at 200 nm.

For wavelength > 120 nm, it is not possible to see the solar events. At short wavelength ~10–20 nm, it could be possible to see the signature of the solar events.

The ozone layer interacts with the UV SSI, hereby heating the lower stratosphere. The SSI variability at 205 nm is important for the ozone chemical budget throughout the stratosphere [40]. This can modulate the UV observed at the ground. The anti-correlation between the TOC (Total Ozone Column) and the UV index measured at the ground during clear sky is greatly visible in the campaign of Athens, as illustrated in Figure 17. The correlation coefficient reaches −0.91. The best linear regression illustrated by the black dashed line in Figure 17 corresponds to UVi = −0.0153*TOC + 8.0238. Less ozone leads to more UV measured at the ground, although the interactions of the UV with clouds and aerosols also play a role.

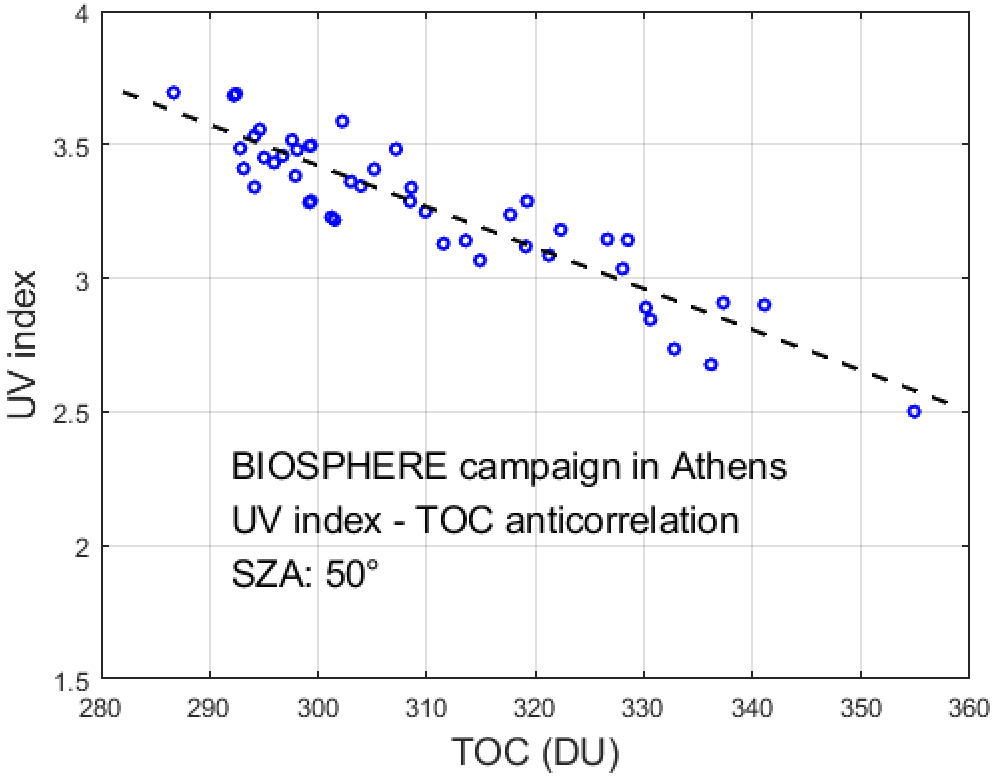

Figure 17. Anti-correlation between the TOC (Total Ozone Column) and the UV index measured at the ground with a solar zenith angle (SZA) of 50° during the campaign of Athens from 1 June 2023 to 31 August 2023.

8. UV and Ozone observed at the ground

The UV monitoring station operated by the Royal Meteorological Institute of Belgium (50.8° N, 4.3° E, 100 m above sea level) is equipped with two Brewer ozone spectrophotometers (#016 since 1984 and #178 since 2002 [41]). The instruments are integrated in the European network EuBrewNet ([42], link to the website and data in section “Data availability” below), in the World Ozone and

Ultraviolet Radiation Data Centre (WOUDC) and in the Network for the Detection of Atmospheric Composition Change (NDACC, Brewer #016). The instruments perform UV scans with constant wavelength steps of 0.5 nm, from 290 nm to 325 nm (Brewer #016) and from 287.5 nm to 363 nm (Brewer #178). For wavelengths above 325 nm (363 nm, respectively), the irradiance values are extrapolated using a theoretical spectrum [43] weighted by the intensity at 325 nm (363 nm, respectively). Brewer #016 and Brewer #178 are calibrated each second year against a NIST traceable 1000W DXW lamp. The total standard uncertainty of the Brewer UV measurements is better than ± 5%. Here, we present time series of the measured daily maximum UV index and the daily average of TOC, measured by Brewer #016 for the period from 1 January to 31 May 2024. Brewer #016 was chosen because Brewer #178 had hardware issues during May 2024 and therefore no complete time series.

Figure 18a and 18b show the measured daily maximum UV index and the daily average total atmospheric ozone content (TOC) for 1 January 2024 to 31 May 2024. The daily maximum UV index increased steadily with increasing solar zenith angle over the course of the time, from values near 0 in January to values of around 5 in May 2024 (peaks on 10 and 11 May 2024 of 5.8). TOC showed high variability with no clear increasing or decreasing tendency, ranging between 271 DU (Dobson Unit) (14 March 2024) to 499 DU (23 February 2024). TOC at Brussels measurement site is during this period strongly influenced on the horizontal displacement of the Arctic polar vortex and related atmospheric circulation patterns. It is nevertheless very interesting to note that the maximum of UV appears on 10–11 May (corresponding to the Mother’s Day), and is associated to a local minimum of TOC. The UV index measured at ground is even larger that the seasonal increase of UV for the month of May.

In the following, we investigate if the lower TOC during these days might be partially due to the arrival of solar energetic particles causing the Mother’s Day geomagnetic storm and is associated with a maximum of UV, both at the ground and in space due to the presence of the active region on the solar disc.

Therefore, we look at total ozone maps above the Northern Hemisphere around 11 May 2024 (Figure 19). From these plots, it is clear that the general circulation is the dominant source of the ozone variability around this time period. In particular, this atmospheric circulation is responsible for a total ozone local minimum around Uccle on 11 May. It is crucial to identify to which extent the additional ozone depletion via the cosmic ray cascade plays a role, so that this minimum around Uccle can be deepened, which requires more model analysis and vertical profiles of ozone.

Due to the strong change in solar zenith angle and respective change in daily maximum UV index values, two scatter plots for the relation between TOC and daily maximum UV index are shown in Figure 20, one for the period 1 January 2024 to 15 March 2024 (upper panel), and one for 16 March 2024 to 31 May 2024 (bottom panel). During the first period, there was no clear relation to be seen between TOC and the daily maximum UV index. During the second period, the tendency for lower daily maximum UV index values to correspond with higher TOC values was more pronounced. The linear correlation factor (r) between the daily average TOC and the daily maxima of UV index (UV index as function of TOC) was 0.0024 (statistically not significant) for the period 2 January to 15 March and −0.39 (statistically significant) for the period 16 March to 31 May 2024. However, besides TOC, other factors influence the maximum UV index, like global solar radiation, cloud cover, and aerosol optical depth (see e.g., [41]).

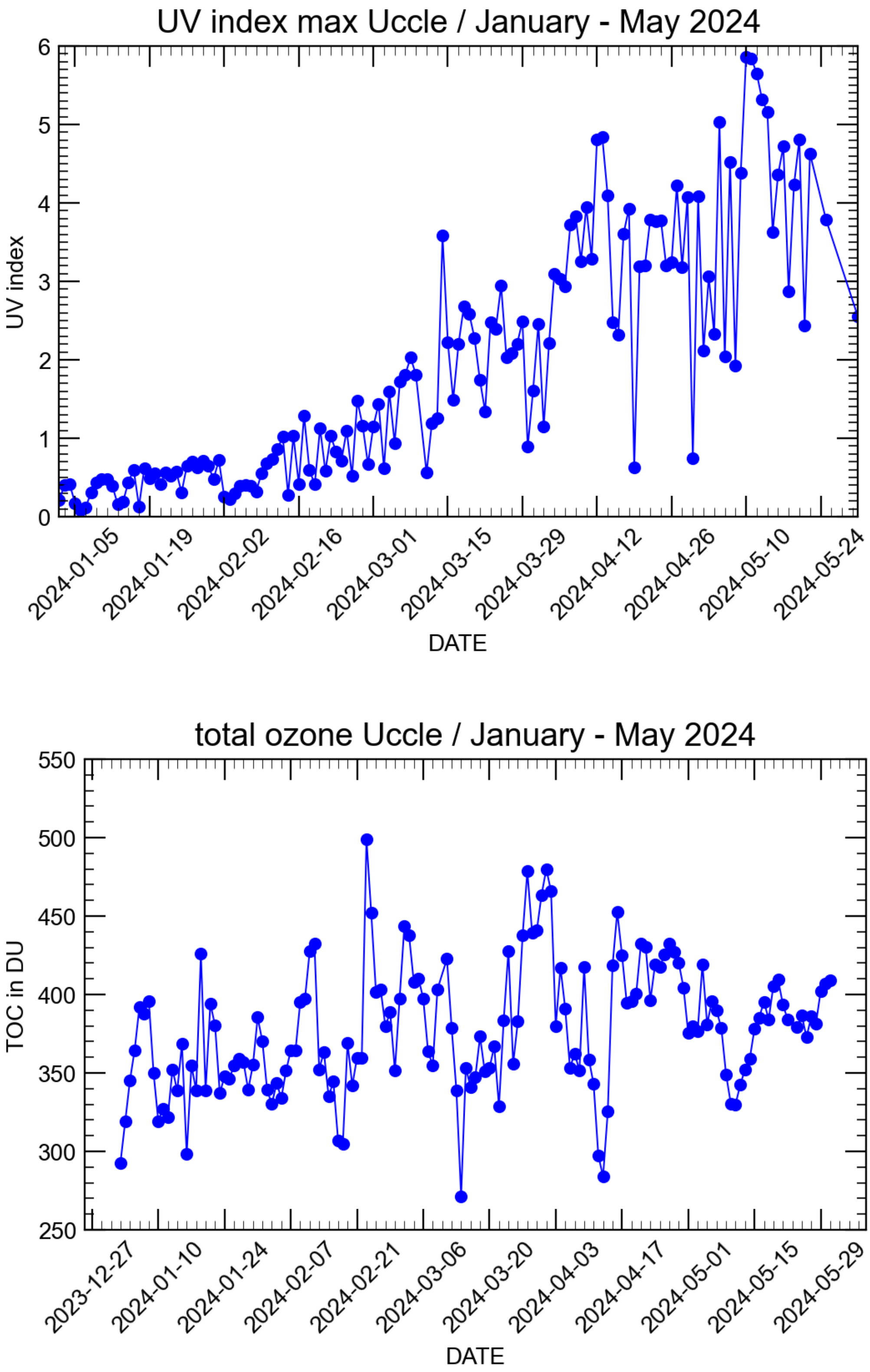

Figure 18. a) Daily maximum UV index for 1 January to 31 May 2024, and b) daily average Total Ozone Content (TOC) for 1 January to 31 May 2024, both measured by Brewer #016 at Uccle (Brussels), Belgium.

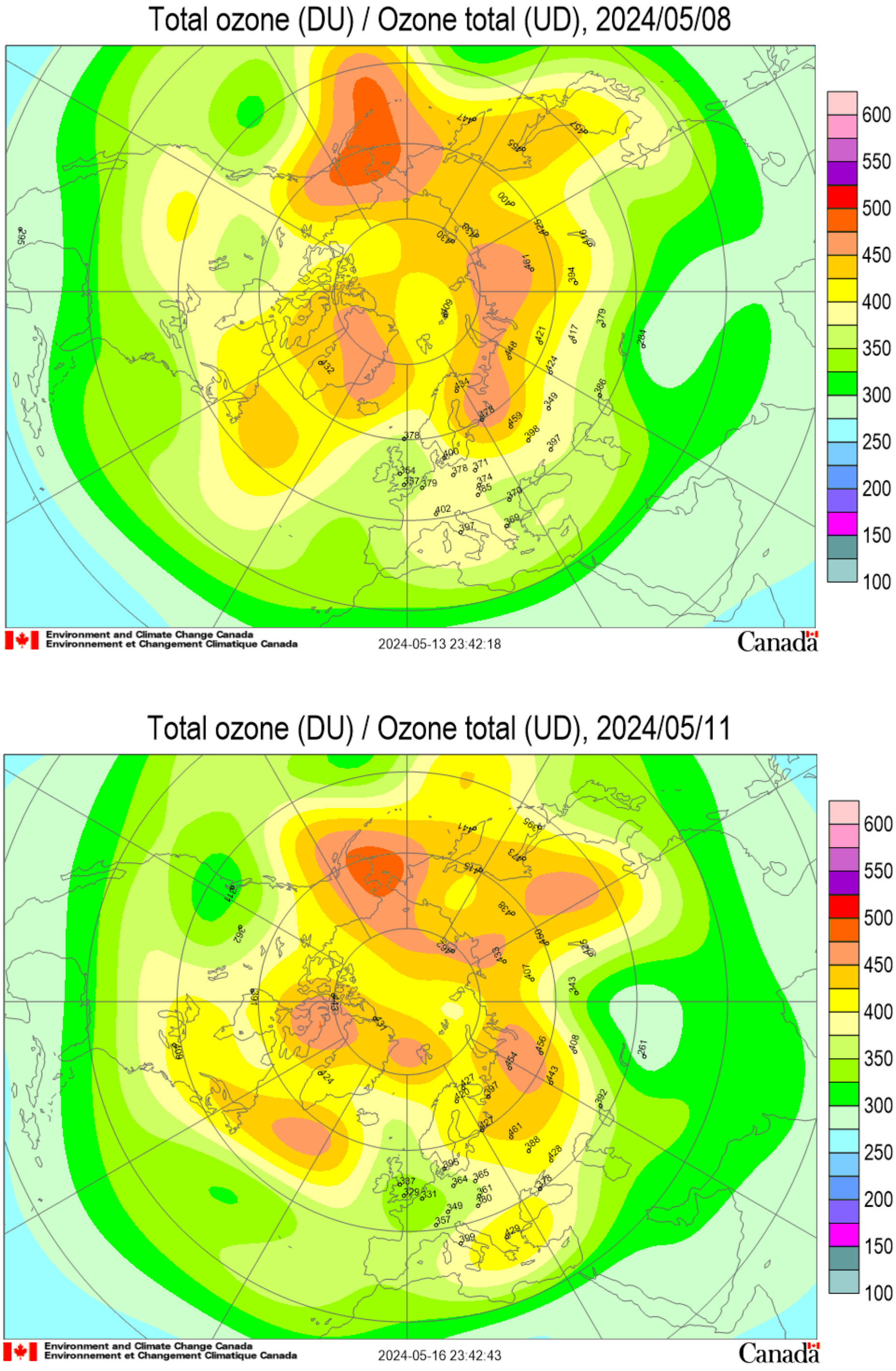
Total ozone (DU) / Ozone total (UD), 2024/05/08

Total ozone (DU) / Ozone total (UD), 2024/05/11

Figure 19. Total Ozone maps above the North pole obtained from WOUDC (World Ozone and Ultraviolet Radiation Data Centre) on 8 May 2024 (upper panel, before the storm) and on 11 May 2024 (bottom panel, during the storm) when a temporally minimum is observed above Belgium.

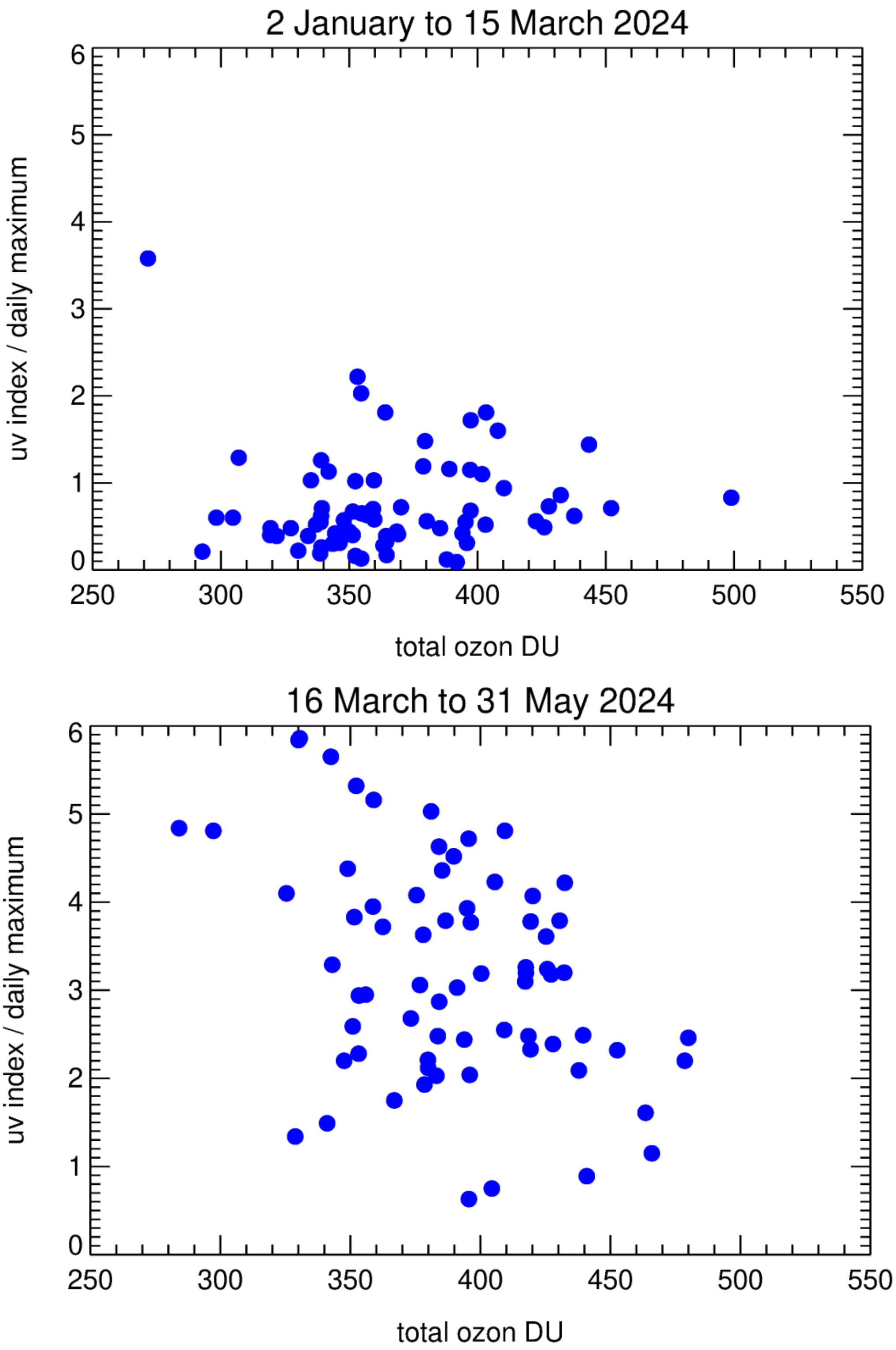

Figure 20. Relation between daily average of TOC and daily maximum UV index, for a) the period 2 January 2024 to 15 March 2024 (upper panel), and for b) the period 16 March 2024 to 31 May 2024 (bottom panel), as measured by Brewer #016 at Uccle, Belgium.

9. Effects on health

The shortest wavelengths (UV, X and γ-rays) are considered the most dangerous for health because they are more energetic and interact more significantly with biological matter leading in most cases to detrimental effects like DNA damage, cell death, and genomic instability. For UV radiation, subdivided into three wavelength bands UV-A (315 nm to 400 nm), UV-B (280 nm to 315 nm), and UV-C (220 nm to 280 nm), the most energetic UV-C are almost completely absorbed by stratospheric ozone before reaching the Earth's surface. Nevertheless, the amount of residual UV-B and UV-A that manages to cross the natural barrier of the atmosphere is far from negligible and can cause sunburn [5]. UV-A is less filtered by the ozone, water vapor, oxygen, and carbon dioxide of the atmosphere than UV-B and UV-C. Clouds reduce the amount of ultraviolet A and B radiation that reaches the Earth's surface and our skin, but is far from stops the damaging rays. Clouds are generally better at blocking visible light than UV.

The effects of solar radiation on human health may be acute or delayed. They may be positive or negative. In any case, humans have developed adaptive inner mechanisms that counterbalance extrinsic disturbances (homeostatic mechanisms), at least to a certain extent.

Solar activity impact on health is a burgeoning scientific field, extending from the biological clock, human chronopathology and epidemiology to chronomics, spatial events, and accidental events. Literature includes reports of solar activity indices (total solar irradiance, sunspot numbers, planetary geomagnetic indices Kp, Ap, and aa, solar flares, neutrons, muons) associations with morbidity and mortality of vital chronic diseases [44–47].

Cyclic variations of intrinsic functions (biological clock: Infradian, ultradian, circaseptan, circadian, annual rhythms) and chronic diseases admittances and mortality have also been reported, insofar [48–50]. Notably, a novel non anthropogenic chronome of 6.8 days in sunspot numbers and stroke incidence has been unraveled [50] (Figure 21). Increase in violence, suicide, and crime fluxes have also been hypothesized to be associated to solar wind and geomagnetic storms [49,51–53]. Different earlier studies show that during periods of severe geomagnetic disturbances, the psycho-neurological patients' hospitalizations increase significantly. On the other hand, cyclic variations of 2 years, 3, and 6 months in ozone concentration and cardiac infractions incidence have also been observed [54]. In Figure 21, the solar, ozone and human major human chronic morbid entities cycles are summarized. Cyclic cardiovascular, cancer, stroke mortality, and cardiovascular, cancer, stroke, and respiratory morbidity follow solar and/or ozone patterns. Delayed periods of 1–2 months for cancer events, 2 months for stroke deaths, and 2 years of cardiovascular deaths were observed [55] (Figure 21).

Concerning stratospheric ozone density variation during solar flares fluxes, respiratory effects and augmented hospital admittances in Sotiria Hospital in Greece coincided with the proton and electron flux on 28 October 2003 [54]. Two retrospective studies on 1955–1962 and 1985–1989 time periods showed that acute events, such as geomagnetic storms (1–2 day observations) and maximum and/or minimum solar activity, are related to an increased ozone variation, by ionizing the stratosphere, and to respiratory morbidity, while strong negative correlation were found between cyclic variations of solar activity and ozone. Acute events like coronal mass ejections and geomagnetic storms contribute to ionization of the atmosphere and have human health respiratory effects. While ozone variation aligns with respiratory hospitalizations, it is inversely correlated to cardiovascular deaths [54].

The impact of mesospheric ozone depletion during solar events on health is expected to be low because the mesospheric ozone anyway disappears during spring in each hemisphere and accounts for a small part of TOC. For UV, the maximum ionization appears during the day close to the equator and at altitude between 200 km and 400 km corresponding to the ionosphere. For energetic particles, the maximum ionization is at high latitude, where the particles are deviated by the terrestrial magnetic field that protects humans. The atmosphere also protects fauna, including humans, so that very few particles can reach the surface of the Earth. Cosmic rays can penetrate at altitudes as low as 10 km and are thus significant for crews and passengers of aviation flights. The particle fluxes can also ionize the atmosphere and modify the concentration of some constituents.

Cosmic rays may enhance aging, notwithstanding the Earth's atmosphere and magnetic field protection [45]. Geomagnetic storms are rare, and most medical emergencies and demises are observed on days of low geomagnetic activity coinciding with increased neutron activity [56]. An earlier epidemiology study on 11-year solar cycle peaks had shown that geomagnetic storms may predispose humans to disease. More specifically, radiation peaks in solar cycles and, particularly in chaotic solar cycles, are associated with a higher incidence of mental disorders, suggesting the sensitivity of ectodermal embryonic tissues to UV radiation (UVR). Autoimmune diseases have intermediate sensitivity, while the neoplasms in the study of [57], primarily of endoderm, appear suppressed by peak UVR intensity.

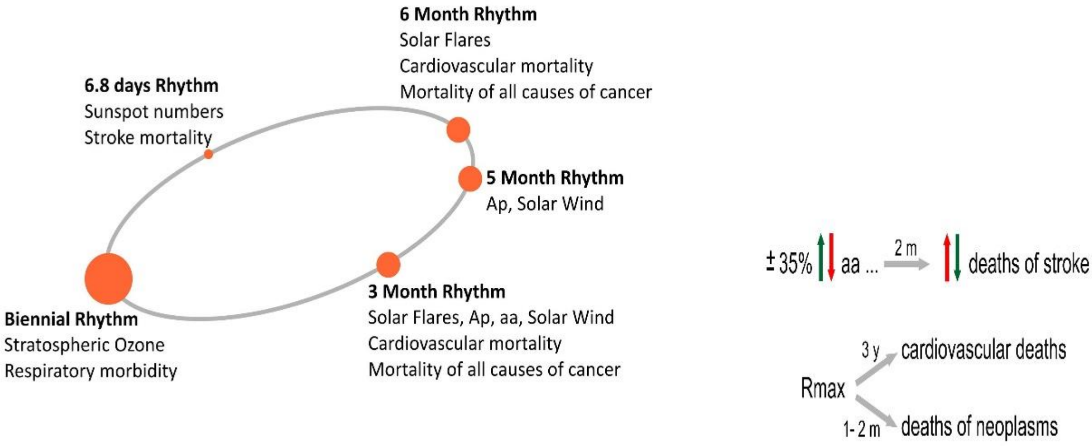

Figure 21. Summary of the solar, ozone, and chronic diseases cycles and delays (incubation periods of diseases). R_{max} corresponds to the date when the sunspot numbers reach maximum; aa is a daily and half-daily index of geomagnetic activity determined from the k indices (A 3-hourly planetary index of geomagnetic activity calculated by the Institut fur Geophysik der Gottingen Universitat, Germany) scaled at two nearly antipodal stations at invariant magnetic latitude 50 degrees. Ap is the earliest occurring maximum 24-hour value obtained by computing an 8-point running average of successive 3-hour ap indices during a geomagnetic storm event and is uniquely associated with the storm event.

Geomagnetic storms and high-speed solar wind (solar wind speed ≥ 600 km/s) and space weather changes prior to solar proton events affect the cardiovascular function [46,47]. There is evidence that more chronic diseases are affected by solar and geomagnetic activity disturbances (i.e., multiple sclerosis, strokes, hypertension, systemic lupus erythematosus, and cancer) [44,49,52,58]. More specifically, it has been suggested that in the mid-latitudes, myocardial infractions may be attributed to the Pc1 geomagnetic pulsations, but in the high latitudes (in maxima of heliogeophysical storminess), this may be attributed to the geomagnetic storminess (indexed by Kp) caused by the solar wind and the interplanetary magnetic field parameters [52,59,60]. Researchers who conducted an epidemiological study concluded that geomagnetic disturbances driven by solar activity enhance total and cardiovascular mortality risk in 263 U.S. cities [61].

More importantly, all these radiation influences have a common, underlying molecular mechanism: The nuclear steroid receptors interactions (R1). This molecular network was generated and functionally preserved over thousands of years across species (thus preserved in evolution of species over time), as the Sun constantly radiated our planet [44,62]. Interestingly, this mechanism disturbance explains all biological effects on humans after exposure to ionizing and non-ionizing radiations.

10. Conclusions

The BIOSPHERE campaign of Brussels enabled us to measure the effects of solar electromagnetic radiation (UV), solar particle radiation (mainly protons and electrons using PROBA-V/EPT at LEO and GOES at geostationary orbit), and ozone simultaneously during a period of 3 months from 1 January 2024 to 31 March 2024 corresponding to maximum solar activity. Seven Solar Energetic Proton events with E > 10 MeV were detected, and three solar and geomagnetic events had different consequences:

1) A Solar Energetic Particle (SEP) event with E > 30 MeV without geomagnetic storm (8 February 2024);
2) A geomagnetic storm without any SEP (3 March 2024);
3) A SEP with E > 30 MeV associated to a geomagnetic storm (24 March 2024).

A FD of the neutrons and of the muons was observed only during this last event during the campaign, and later during the Mother’s Day on 11 May 2024, generating the most intense geomagnetic storm for the last 20 years. The measurements show that ozone in the mesosphere, present during the winter in the Northern hemisphere, is lost during some SEP events, and especially during the Mother’s Day event on 11 May 2024 [9]. The stratosphere can also be affected but a longer period of observations would be necessary to obtain clear conclusions since so many other effects influence stratospheric ozone. The geomagnetic storms affect more the electrons of the radiation belts.

The particle injections (solar protons, energetic electrons from the radiation belts or aurora, and cosmic rays) are limited to high latitudes except during strong magnetic storms when lower latitudes can be affected. GCRs ionize at lower altitudes around 10 km corresponding to airplanes altitudes, because they carry the most energetic particles that can penetrate deeper.

Equatorial regions are more ionized by UV radiation during the day at higher altitudes with a maximum between 200 km and 400 km. In space, the UV solar radiation shows not only the well-known solar cycle variation of 11 years, but also a cycle of 27 days (like the solar activity indices) well visible during the first months of 2024 due to the solar rotation of the Sun on itself, leading to active regions coming back in the direction of the Earth.

The AtRIS model confirms the ionization rate depending on the energy of the particles and the altitude. Solar protons can penetrate at 50 km in the stratosphere. In addition to ionization, the particles can modify the composition of the atmosphere by chemical reactions (ozone, NOx, HOx, etc.) and the temperature by heating, producing thermal expansion of the atmosphere.

Such rare simultaneous observations of solar UV, solar eruptions, and geomagnetic storms give new important results concerning the effects on the atmosphere of each independent source. This is crucial since acute events, such as solar eruptions (1–2 day observations) and maximum and/or minimum solar activity, are related to ozone variations by ionizing the atmosphere and to potential health effects.

Acknowledgements

The authors acknowledge the project 21GRD02 BIOSPHERE from the European Partnership on Metrology. The project (21GRD02 BIOSPHERE) has received funding from the European Partnership on Metrology, co-financed from the European Union’s Horizon Europe Research and Innovation Programme and by the Participating States. VP, AW and EB thank the Horizon 2020 research and innovation programme funding from the European Union for the PITHIA-NRF project (Plasmasphere Ionosphere Thermosphere Integrated Research Environment and Access services) with Grant Agreement 101007599. Work at VSB TU Ostrava was supported by the project SGS SP 2024/016 at the VSB TU Ostrava financed by the Ministry of Education, Youth and Sports of the Czech Republic. JoeySAT has been developed under the Sunrise Partnership Project between ESA and telecommunications operator OneWeb, with support from the UK Space Agency.

Data availability

The data presented in this study are available in a repository at DOI reference number https://doi.org/10.5281/zenodo.14390477. These data were derived from the following resources. Available in the public domain:

Omni data are provided by https://omniweb.gsfc.nasa.gov/html/ow_data.html. Sunspot number data can be downloaded from http://www.sidc.be/silso/datafiles/. Dst data was retrieved from https://wdc.kugi.kyoto-u.ac.jp/. GOES data are accessible at https://lasp.colorado.edu/space-weather-portal/. MLS/Aura data of ozone are accessible at https://disc.gsfc100.nasa.gov/datasets/ML2O3_005/summary, using recommendations for data screening provided in the MLS Level 2 Version 5 Quality Document https://mls.jpl.nasa.gov/data/v5-0 data quality document.pdf). EPT data are publicly available on the Space Situational Awareness website of ESA http://swe.ssa.esa.int/space-radiation.

Solar Spectral Irradiance (SSI) measured by TSIS-1 come from https://lasp.colorado.edu/tsis/data/. Total ozone and UV measurements are available on Eubrewnet (https://eubrewnet.aemet.es/eubrewnet) and WOUDC (woudc.org). Ozone maps are available on WOUDC - World Ozone and Ultraviolet Radiation Data Centre (woudc.org).

Data of the BIOSPHERE project as well as two Good Practice Guides (1. for the Analysis of Space Radiation Fluxes and Simulations of their Interactions with the Atmosphere, including AtRIS, and 2. Effects of combined Secondary Cosmic Rays and UV radiation fields on biological systems) are available on euramet-biosphere.eu/publications.

Results presented in this document rely on data provided by the Community Coordinated Modeling Center at Goddard Space Flight Center through their integrated Space Weather Analysis (iSWA) system's HAPI server (https://iswa.gsfc.nasa.gov/IswaSystemWebApp/hapi). The CCMC is a multi-agency partnership between NASA, AFMC, AFOSR, AFRL, AFWA, NOAA, NSF and ONR. These data were accessed via the University of Colorado's Space Weather Technology, Research, and Education Center's (https://colorado.edu/spaceweather) Space Weather Data Portal (https://lasp.colorado.edu/space-weather-portal).

Author contributions

Conceptualization, VP, DB, and FK; methodology, VP; software, all; validation, VP, DB, FK; formal analysis, all authors; investigation, all; resources, FK, DB; data curation, AW; writing–original draft preparation, VP; writing–review and editing, all; visualization, all; supervision, VP; project administration, FK; funding acquisition, FK. All authors have read and agreed to the present version of the manuscript.

Use of AI tools declaration

The authors declare they have not used Artificial Intelligence (AI) tools in the creation of this article.

Conflict of Interest

The authors declare no conflicts of interest.

References

1. Sinnhuber M, Nieder H, Wieters N (2012) Energetic Particle Precipitation and the Chemistry of the Mesosphere/Lower Thermosphere. *Surv Geophys* 33: 1281–1334. https://doi.org/10.1007/s10712-012-9201-3
2. Krasniqi F (2023) Biosphere Newsletter, 1st issue. Available from: www.euramet-biosphere.eu.
3. Papayannis A, Gidarakou M, Mylonaki M, et al. (2023) Aerosol, Temperature and Water Vapor profiling during the BIOSPHERE Athens Campaign (June-August 2023). 4th European Lidar Conference, Cluj-Napoca, Romania. https://doi.org/10.5281/zenodo.10018507
4. Pierrard V, Lopez Rosson G, Borremans K, et al. (2014) The Energetic Particle Telescope: First results. *Space Sci Rev* 184: 87–106. https://doi.org/10.1007/s11214-014-0097-8
5. Pierrard V (2024) *Effects of the Sun on the space environment of the Earth*, Presses Universitaires de Louvain, 208. https://i6doc.com/en/book/?gcoi=28001100628290

6. Evans D, Greer M (2000) Polar orbiting environmental satellite space environment monitor. NOAA National Geophysical Data Center.
7. Schwartz M, Froidevaux L, Livesey N, et al. (2020) MLS/Aura Level 2 Ozone (O3) Mixing Ratio V005, Greenbelt, MD, USA, Goddard Earth Sciences Data and Information Services Center (GES DISC).
8. Smith AK, Espy PJ, Lopez-Puertas M, et al. (2018) Spatial and temporal structure of the tertiary ozone maximum in the polar winter mesosphere. *J Geophys Res Atmos* 123: 4373–4389. https://doi.org/10.1029/2017JD028030
9. Winant A, Pierrard V, Botek E (2025) Ozone decrease observed in the upper atmosphere following the May 11th 2024 *Mother's Day* solar storm. *Ann Geophys Discuss*. [preprint]. https://doi.org/10.5194/angeo-2024-29
10. Banjac S, Herbst K, Heber B (2019) The atmospheric radiation interaction simulator (AtRIS): Description and validation. *J Geophys Res Space Phys* 124: 50–67. https://doi.org/10.1029/2018JA026042
11. Winant A, Pierrard V, Botek E, et al. (2023) The atmospheric influence on cosmic ray induced ionization and absorbed dose rates. *Universe* 9: 502. https://doi.org/10.3390/universe9120502
12. Bilitza D, Pezzopane M, Truhlik V, et al. (2022) The International Reference Ionosphere model: A review and description of an ionospheric benchmark. *Rev Geophys* 60: e2022RG000792. https://doi.org/10.1029/2022RG000792
13. Pierrard V, Botek E, Darrouzet F (2021) Improving Predictions of the 3rd Dynamic Model of the Plasmasphere. *Front Astron Space Sci* 8: 681401. https://doi.org/10.3389/fspas.2021.681401
14. Andersson ME, Verronen PT, Wang S, et al. (2012) Precipitating radiation belt electrons and enhancements of mesospheric hydroxyl during 2004–2009. *J Geophys Res Atmos* 117. https://doi.org/10.1029/2011JD017246
15. Wolff W, Dogan M, Luna H, et al. (2024) Absolute electron impact ionization cross-sections for CF4: Three dimensional recoil-ion imaging combined with the relative flow technique. *Rev Sci Instrum* 95: 095103. https://doi.org/10.1063/5.0219527
16. Cyamukungu M, Benck S, Borisov S, et al. (2014) The Energetic Particle Telescope (EPT) on board PROBA-V: description of a new science-class instrument for particle detection in space. *IEEE Trans Nucl Sci* 61: 3667–3681. https://doi.org/10.1109/TNS.2014.2361955
17. McIlwain CE (1966) Magnetic coordinates. *Space Sci Rev* 5: 585–598. https://doi.org/10.1007/BF00167327
18. Pierrard V, Botek E, Ripoll JF, et al. (2020) Electron dropout events and flux enhancements associated with geomagnetic storms observed by PROBA-V/EPT from 2013 to 2019. *J Geophys Res Space Phys* 125: e2020JA028487. https://doi.org/10.1029/2020JA028487
19. Pierrard V, Lopez Rosson G (2016) The effects of the big storm events in the first half of 2015 on the radiation belts observed by EPT/PROBA-V. *Ann Geophys* 34: 75–84. https://doi.org/10.5194/angeo-34-75-2016
20. Pierrard V, Ripoll J-F, Cunningham G, et al. (2021) Observations and simulations of dropout events and flux enhancements in October 2013: Comparing MEO equatorial with LEO polar orbit. *J Geophys Res Space Phys* 126: e2020JA028850. https://doi.org/10.1029/2020JA028850

21. Pierrard V, Botek E, Ripoll J-F, et al. (2021) Links of the plasmapause with other boundary layers of the magnetosphere: ionospheric convection, radiation belts boundaries, auroral oval. *Front Astron Space Sci* 8. https://doi.org/10.3389/fspas.2021.728531
22. Cunningham GS, Botek E, Pierrard V, et al. (2020) Observation of High-Energy Electrons Precipitated by NWC Transmitter from PROBA-V Low-Earth Orbit Satellite. *Geophys Res Lett* 47: e2020GL089077. https://doi.org/10.1029/2020GL089077
23. Botek E, Pierrard V, Winant A (2023) Prediction of radiation belts electron fluxes at a Low Earth Orbit using neural networks with PROBA-V/EPT data. *Space Weather* 21: e2023SW003466. https://doi.org/10.1029/2023SW003466
24. Girgis KM, Hada T, Yoshikawa A, et al. (2023) Geomagnetic Storm Effects on the LEO Proton Flux during Solar Energetic Particle Events. *Space Weather* 21: e2023SW003664. https://doi.org/10.1029/2023SW003664
25. Pierrard V, Benck S, Botek E, et al. (2023) Proton flux variations during Solar Energetic Particle Events, minimum and maximum solar activity and splitting of the proton belt in the South Atlantic Anomaly. *J Geophys Res Space Phys* 128: e2022JA031202. https://doi.org/10.1029/2022JA031202
26. Pierrard V, Winant A, Botek E, et al. (2024) The Mother's Day solar storm of 11 May 2024 and its effect on Earth's radiation belts. *Universe* 10: 391. https://doi.org/10.3390/universe10100391
27. Poikela T, Plosila J, Westerlund T, et al. (2014) Timepix3: a 65K channel hybrid pixel readout chip with simultaneous ToA/ToT and sparse readout. *J Instrum* 9: C05013. https://doi.org/10.1088/1748-0221/9/05/C05013
28. Freiherr von Forstner JL, Dumbović M, Möstl C, et al. (2021) Radial evolution of the April 2020 stealth coronal mass ejection between 0.8 and 1 AU. Comparison of Forbush decreases at Solar Orbiter and near the Earth. *Astron Astrophys* 656. https://doi.org/10.1051/0004-6361/202039848
29. Krasniqi F, Stolzenberg U, Luchkov M, et al. (2022) PTB metrological infrastructure for the environmental dose assessment. *PTB-Mitt* 132: 21–31.
30. Chilingarian A, Hovsepyan G, Arakelyan K, et al. (2009) Space environmental viewing and analysis network (SEVAN). *Earth Moon Planets* 104: 195. https://doi.org/10.1007/s11038-008-9288-1
31. Chilingarian A, Babayan V, Karapetyan T, et al. (2018) The SEVAN Worldwide network of particle detectors: 10 years of operation. *Adv Space Res* 61: 2680–2696. https://doi.org/10.1016/j.asr.2018.02.030
32. Granja C, Jakubek J, Soukup P, et al. (2022) Spectral tracking of energetic charged particles in wide field-of-view with miniaturized telescope MiniPIX Timepix3 1 × 2 Stack. *J Instrum* 17: C03028. https://doi.org/10.1088/1748-0221/17/03/C03028
33. Granja C, Pospisil S (2014) Quantum Dosimetry and Online Visualization of X-ray and Charged Particle Radiation in Aircraft at Operational Flight Altitudes with the Pixel Detector Timepix. *Adv Space Res* 54: 241–251. https://doi.org/10.1016/j.asr.2014.04.006
34. Spogli L, Alberti T, Bagiacchi P, et al. (2024) The effects of the May 2024 Mother's Day superstorm over the Mediterranean sector: from data to public communication. *Ann Geophys* 67: PA218. https://doi.org/10.4401/ag-9117

35. Themens DR, Elvidge S, McCaffrey A, et al. (2024) The high latitude ionospheric response to the major May 2024 geomagnetic storm: A synoptic view. *Geophys Res Lett* 51: e2024GL111677. https://doi.org/10.1029/2024GL111677
36. Pierrard V, Verhulst TGW, Chevalier J-M, et al. (2025) Effects of the geomagnetic superstorms of 10–11 May 2024 and 7–11 October 2024 on the ionosphere and plasmasphere. *Atmosphere* 16: 299. https://doi.org/10.3390/atmos16030299
37. Liu X, Xu J, Yue J, et al. (2025) Mesosphere and lower thermosphere temperature responses to the May 2024 Mother's Day storm. *Geophys Res Lett* 52: e2024GL112179. https://doi.org/10.1029/2024GL112179
38. Richard E, Harber D, Coddington O, et al. (2020) SI-traceable spectral irradiance radiometric characterization and absolute calibration of the TSIS-1 spectral irradiance monitor (SIM). *Remote Sens* 12: 1818. https://doi.org/10.3390/rs12111818
39. DeLand MT, Cebula RP (1993) Composite MgII solar activity index for solar cycles 21 and 22. *J Geophys Res Atmos* 98: 12809–12823. https://doi.org/10.1029/93JD00421
40. Bossay S (2015) Impact de la variabilité solaire sur l’ozone de la moyenne atmosphère. PhD Thesis, Université Versailles Saint Quentin en Yvelines, France. https://theses.hal.science/tel-01139519/
41. De Bock V, De Backer H, Van Malderen R, et al. (2014) Relations between erythemal UV dose, global solar radiation, total ozone column and aerosol optical depth at Uccle, Belgium. *Atmos Chem Phys* 14: 12251–12270. https://doi.org/10.5194/acp-14-12251-2014
42. Rimmer JS, Redondas A, Karppinen T (2018) EuBrewNet—A European Brewer network (COST Action ES1207), an overview. *Atmos Chem Phys* 18: 10347–10353. https://doi.org/10.5194/acp-18-10347-2018
43. McKinlay AF, Diffey BL (1987) A Reference Action Spectrum for Ultraviolet Induced Erythema in Human Skin. *CIE J* 6: 17–22. International Organization for Standardization and International Commission on Illumination. Erythema reference action spectrum and standard erythema dose (ISO/CIE 17166:2019). Available from: https://www.iso.org.
44. Geronikolou S, Zimeras S, Tsitomeneas S, et al. (2023) Total Solar Irradiance and Stroke Mortality by Neural Networks Modelling. *Atmosphere* 14: 114. https://doi.org/10.3390/atmos14010114
45. Zhai T, Zilli Vieira CL, Vokonas P, et al. (2024) Annual space weather fluctuations and telomere length dynamics in a longitudinal cohort of older men: the Normative Aging Study. *J Expo Sci Environ Epidemiol* 34: 1072–1080. https://doi.org/10.1038/s41370-023-00616-z
46. Vencloviene J, Babarskiene RM, Kiznys D (2017) A possible association between space weather conditions and the risk of acute coronary syndrome in patients with diabetes and the metabolic syndrome. *Int J Biometeorol* 61: 159–167. https://doi.org/10.1007/s00484-016-1200-5
47. Zilli Vieira CL, Chen K, Garshick E, et al. (2022) Geomagnetic disturbances reduce heart rate variability in the Normative Aging Study. *Sci Total Environ* 839: 156235. https://doi.org/10.1016/j.scitotenv.2022.156235
48. Halberg F, Cornélissen G, Katinas G, et al. (2007) Chronomics and Genetics. *Scr Med (Brno)* 80: 133–150.
49. Halberg F, Cornélissen G, Katinas GS, et al. (2010) Cosmic Inheritance Rules: Implications for Health Care and Science. *Scr Med (Brno)* 83: 5–15

50. Geronikolou S, Leontitsis A, Petropoulos V, et al. (2020) Cyclic stroke mortality variations follow sunspot patterns. *F1000Research* 9: 1088. https://doi.org/10.12688/f1000research.24794.2
51. Persinger MA (1997) Geomagnetic variables and behavior: LXXXIII. Increased geomagnetic activity and group aggression in chronic limbic epileptic male rats. *Percept Motor Skill* 85(3_suppl): 1376–1378. https://doi.org/10.2466/pms.1997.85.3f.1376
52. Halberg F, Siutkina EV, Cornelissen G (1998) Chronomes render predictable the otherwise-neglected human "physiological range": position paper of the BIOCOS project, BIOsphere and the COSmos. *Fiziologiia Chel* 24: 14–21.
53. Mulligan B, Koren S (2021) Geopsychology of instrumental aggression: daily concurrence of global terrorism and solar-geomagnetic activity (1970–2018). *Adv Soc Sci Res J* 8: 487–499. https://doi.org/10.14738/assrj.85.10266
54. Geronikolou S, Petropoulos V (2005) Stratospheric ozone, density variation solar activity and biological phenomena. HELLASET International Congress Cephalonia.
55. Geronikolou SA (2014) Evaluation of chronomes in the Greek population and their relation to solar and atmospheric activity cycles, *The Mediterranean City 2014 Proceedings*, Mariolopoulos-Kanaginis Foundation, 16–17.
56. Stoupel E (2015) Considering space weather forces interaction on human health: the equilibrium paradigm in clinical cosmobiology—is it equal? *J Basic Clin Physiol Pharmacol* 26: 147–151. https://doi.org/10.1515/jbcpp-2014-0059
57. Davis GE, Lowell WE (2006) Solar cycles and their relationship to human disease and adaptability. *Med Hypotheses* 67: 447–461. https://doi.org/10.1016/j.mehy.2006.03.011
58. Papathanasopoulos P, Preka-Papadema P, Gkotsinas A, et al. (2016) The possible effects of the solar and geomagnetic activity on multiple sclerosis. *Clin Neurol Neurosurg* 146: 82–89. https://doi.org/10.1016/j.clineuro.2016.04.023
59. Halberg F, Cornélissen G, Otsuka K, et al. (2000) Cross-spectrally coherent ~10.5- and 21-year biological and physical cycles, magnetic storms and myocardial infarctions. *Neuro Endocrinol Lett* 21: 233–258.
60. Samsonov SN, Manykina VI, Kleimenova NG, et al. (2016) The HELIO-geophysical storminess health effects in the cardio-vascular system of a human in the middle and high latitudes. *Wiad Lek* 69(3 pt 2): 537–541.
61. Zilli Vieira CL, Alvares D, Blomberg A, et al. (2019) Geomagnetic disturbances driven by solar activity enhance total and cardiovascular mortality risk in 263 U.S. cities. *Environ Health* 18: 83. https://doi.org/10.1186/s12940-019-0516-0
62. Geronikolou SA, Pavlopoulou A, Kanaka-Gantenbein C, et al. (2018) Inter-species functional interactome of nuclear steroid receptors (R1). *Front Biosci (Elite Ed)* 10: 208–228. https://doi.org/10.2741/e818

AIMS Press